

An Efficient Constant-Coefficient MSAV Scheme for Computing Vesicle Growth and Shrinkage

Zhiwei Zhang^a, Shuwang Li^a, John Lowengrub^b, Steven M. Wise^c

^a*Department of Applied Mathematics, Illinois Institute of Technology, Chicago, 60616, IL, USA*

^b*Department of Mathematics, University of California, Irvine, 92697, CA, USA*

^c*Department of Mathematics, The University of Tennessee, Knoxville, 37996, TN, USA*

Abstract

We present a fast, unconditionally energy-stable numerical scheme for simulating vesicle deformation under osmotic pressure using a phase-field approach. The model couples an Allen–Cahn equation for the biomembrane interface with a variable-mobility Cahn–Hilliard equation governing mass exchange across the membrane. Classical approaches, including nonlinear multigrid and Multiple Scalar Auxiliary Variable (MSAV) methods, require iterative solution of variable-coefficient systems at each time step, resulting in substantial computational cost. We introduce a constant-coefficient MSAV (CC-MSAV) scheme that incorporates stabilization directly into the Cahn–Hilliard evolution equation rather than the chemical potential. This reformulation yields fully decoupled constant-coefficient elliptic problems solvable via fast discrete cosine transform (DCT), eliminating iterative solvers entirely. The method achieves $O(N^2 \log N)$ complexity per time step while preserving unconditional energy stability and discrete mass conservation. Numerical experiments verify second-order temporal and spatial accuracy, mass conservation to relative errors below 5×10^{-11} , and close agreement with nonlinear multigrid benchmarks. On grids with $N \geq 2048$, CC-MSAV achieves 6–15× overall speedup compared to classical MSAV with optimized preconditioning, while the dominant Cahn–Hilliard subsystem is accelerated by up to two orders of magnitude. These efficiency gains, achieved without sacrificing accuracy,

Email addresses: `zzhang107@hawk.illinoistech.edu` (Zhiwei Zhang),
`sli15@illinoistech.edu` (Shuwang Li), `jlowengr@uci.edu` (John Lowengrub),
`swise1@utk.edu` (Steven M. Wise)

make CC-MSAV particularly well-suited for large-scale simulations of vesicle dynamics.

Keywords: Cahn-Hilliard equation, Scalar auxiliary variable, Constant-coefficient, Energy stability, Variable mobility, Phase-field method, Vesicle deformation

1. Introduction

Lipid vesicles are closed bilayer membranes enclosing an aqueous volume. These structures form when phospholipid molecules self-assemble in aqueous environments, with hydrophilic heads facing outward and hydrophobic tails forming the interior bilayer. Due to their structural simplicity and rich mechanical behavior, vesicles provide tractable platforms for studying membrane deformation, shape transitions, and transport phenomena relevant to cellular biology [23]. Among the many physical processes governing vesicle behavior, osmotically driven volume change plays a particularly important role: concentration gradients across the semi-permeable membrane induce material transport and subsequent morphological evolution [17, 33, 19]. Understanding how vesicles respond to osmotic stress, whether growing, shrinking, or maintaining equilibrium, is essential for applications ranging from drug delivery systems [7] to synthetic cell design and fundamental biophysics.

Mathematical modeling of vesicle mechanics has evolved along two complementary approaches. Sharp-interface models explicitly track the membrane as a moving interface, satisfying geometric constraints and interface conditions exactly. These methods have successfully captured vesicle dynamics in flow [32, 31, 27, 21, 10], shape transitions under shear [15], and membrane wrinkling phenomena [14, 36]. Phase-field models, alternatively, represent the membrane as a continuous transition layer of small thickness ε , transforming the moving interface problem into coupled reaction-diffusion equations on a fixed domain [6, 34, 16]. The phase-field approach implicitly determines the interface position and offers advantages in computational simplicity, as well as natural handling of topological changes.

Our work builds upon the phase-field vesicle model of Tang et al. [29], which couples Allen-Cahn and Cahn-Hilliard equations to capture membrane evolution and concentration dynamics under osmotic pressure. While their nonlinear multigrid (NLMG) solver achieves first-order temporal accuracy with near-optimal convergence, it requires iterative solution of the coupled

nonlinear system at each time step, incurring substantial computational expense for large-scale simulations.

Several recent developments have enriched the numerical analysis of related phase-field problems. Guo et al. [9] constructed high-order energy-stable discontinuous Galerkin methods for osmotic flow through semi-permeable membranes, and Zhang et al. [24] established existence and regularity results for triplet phase-separation models. For gradient flows, the Scalar Auxiliary Variable (SAV) framework [26], building upon the earlier Invariant Energy Quadratization (IEQ) approach [37], has emerged as an effective tool for constructing energy-stable schemes. SAV introduces auxiliary variables to represent nonlinear energy terms, enabling reformulation of the system into linear problems with constant coefficients while maintaining unconditional energy stability. The Multiple-SAV (MSAV) extension [4] introduces separate auxiliary variables for each nonlinear contribution and serves as the foundation for the present work. However, extending these advantages to Cahn–Hilliard equations with variable mobility is nontrivial and leads to additional structural challenges.

For Cahn–Hilliard equations with variable mobility, applying SAV- and MSAV-type reformulations remains challenging, as unconditional energy stability is often difficult to maintain together with a constant-coefficient, fully decoupled linear structure. In classical SAV and MSAV approaches, stabilization is typically introduced at the level of the chemical potential; when the mobility is variable, this generally leads to linear equations with variable coefficients and thus precludes the constant-coefficient structure of the resulting elliptic problems. Huang et al. [11] developed a structure-preserving upwind-SAV scheme for degenerate mobility that is energy stable; however, the mobility enters the discrete fluxes at the new time level, resulting in mobility-dependent operators rather than constant-coefficient elliptic problems. Bretin et al. [1] showed that straightforward SAV extensions lose Fourier-explicit solvability for degenerate mobilities. To address this, they introduced a mobility-based SAV reformulation in which the implicit operator involves a constant mobility upper bound, yielding constant-coefficient linear subproblems and stability results that rely on auxiliary-variable constraints. By contrast, Orizaga and Witelski [18] proposed IMEX splittings that enable constant-coefficient implicit solves by separating the mobility into constant and variable parts, but unconditional energy stability is not guaranteed in general and holds only for certain parameter choices.

Motivated by these challenges, we introduce a constant-coefficient Multi-

ple Scalar Auxiliary Variable (CC-MSAV) scheme that exploits the specific structure of the coupled Allen–Cahn–Cahn–Hilliard system for vesicle deformation. The model couples an Allen–Cahn equation for the membrane phase field ϕ with a Cahn–Hilliard equation for the concentration field ψ , where variable mobility $M_\psi(\phi)$ introduces coupling between the two equations. Following classical approaches, we treat the mobility through extrapolation to achieve linearity. Our key insight is to reformulate the osmotic coupling such that stabilization can be incorporated directly into the Cahn–Hilliard evolution equation rather than into the chemical potential, which is the standard approach in classical MSAV methods. Specifically, the energy functional decomposes into four components (surface, bending, surface area constraint, and osmotic energy), each with a nonlinear part represented by a separate SAV variable. The osmotic energy, which couples ϕ and ψ , is wrapped entirely within its SAV variable, ensuring that the chemical potential contains no linear differential operators acting on the unknown ψ^{n+1} , such as ψ^{n+1} or $\Delta\psi^{n+1}$. This formulation enables linear stabilization to be incorporated directly into the evolution equation, yielding a fully decoupled system at each time step: five fourth-order equations for the Allen–Cahn subsystem and two second-order equations for the Cahn–Hilliard subsystem, all with constant coefficients. Each equation is solved via discrete cosine transform (DCT), which diagonalizes the discrete Laplacian under homogeneous Neumann boundary conditions and provides fast, machine-precision direct solves with computational complexity $O(N^2 \log N)$ [28, 30, 13, 22].

This constant-coefficient reformulation provides substantial computational advantages over variable-coefficient approaches. At grid resolutions relevant for vesicle simulations ($N \geq 2048$), sparse direct solvers for variable-coefficient elliptic equations become prohibitively expensive due to fill-in during factorization, resulting in superlinear computational complexity and excessive memory usage. Iterative methods such as multigrid or preconditioned Krylov solvers offer improved scalability, but even well-optimized implementations remain significantly slower than fast transform-based solvers available for constant-coefficient operators. When classical MSAV is equipped with a DCT-based Poisson preconditioner, approximately 12–13 Krylov iterations are required per Cahn–Hilliard solve (24–26 per time step). In contrast, the proposed CC-MSAV formulation yields fully decoupled constant-coefficient elliptic problems that are solved directly via DCT with zero iterations. As demonstrated in Section 3.5, this structural simplification leads to 6–15× overall speedup for $N \geq 2048$. Moreover, the Cahn–Hilliard subsystem, which

dominates the computational cost in classical formulations, becomes a minor component of the total runtime under the proposed scheme. This reduction yields order-of-magnitude savings relative to both sparse direct solvers and well-preconditioned iterative methods, without compromising accuracy or unconditional energy stability.

The numerical experiments demonstrate that the proposed CC-MSAV method achieves second-order temporal and spatial accuracy, robust energy decay, and near machine precision mass conservation, with relative errors below 5×10^{-11} . The method performs robustly across a wide range of scenarios, including non-convex geometries (triangles, stars, crescents) involving topological changes. Comparisons with classical MSAV and well-preconditioned iterative methods demonstrate significant reductions in wall-clock time while maintaining agreement with established nonlinear multigrid benchmarks. The combination of unconditional energy stability, second-order accuracy, optimal complexity scaling, and the elimination of iterative solvers makes CC-MSAV particularly well-suited for large-scale computational investigations of vesicle dynamics under osmotic stress.

The remainder of this paper is organized as follows. In Section 2, we present the phase-field model and derive the MSAV reformulation. In Section 3, we present the numerical discretization, prove energy stability, and discuss computational efficiency. In Section 4, we provide comprehensive numerical validation, including convergence studies, benchmark comparisons with NLMG, and robustness demonstrations on complex geometries. In Section 5, we summarize the findings and discuss future research directions. For completeness, in Appendix A we provide the full proof of unconditional energy stability for the proposed CC-MSAV scheme; in Appendix B we give the complete solution procedure for the MSAV–BDF2 system; and in Appendix C we describe the DCT-based fast direct solver used for the constant-coefficient elliptic equations.

2. Mathematical Formulation of the Phase-Field Model

In this section, we present the mathematical formulation of the phase-field vesicle model and its MSAV reformulation. We first recall the model of Tang et al. [29], then introduce an MSAV reformulation that preserves energy dissipation while leading to linear, decoupled, and computationally efficient schemes.

2.1. Phase-Field Vesicle Model

We consider the phase-field vesicle model of Tang et al. [29], which describes vesicle deformation driven by surface tension, bending elasticity, osmotic pressure, and an arc-length conservation constraint. Let $\Omega \subset \mathbb{R}^2$ denote a square computational domain. Two primary fields are defined on Ω : the phase-field variable $\phi(x, t) : \Omega \rightarrow \mathbb{R}$, with $\phi = 1$ inside the vesicle and $\phi = -1$ outside, and the solute concentration $\psi(x, t) : \Omega \rightarrow \mathbb{R}$. The zero level set $\{\mathbf{x} : \phi(\mathbf{x}) = 0\}$ approximates the membrane location.

Governing equations. The system evolves according to coupled Allen–Cahn and Cahn–Hilliard equations, representing gradient flows of a total free energy functional $F[\phi, \psi]$:

$$\frac{\partial \phi}{\partial t} = -M_\phi \mu, \quad (2.1)$$

$$\frac{\partial \psi}{\partial t} = \nabla \cdot (M_\psi(\phi) \nabla \nu), \quad (2.2)$$

where $\mu = \delta F / \delta \phi$ and $\nu = \delta F / \delta \psi$ denote the chemical potentials, whose explicit forms will be derived below. Here $M_\phi > 0$ is constant, while the Cahn–Hilliard mobility $M_\psi(\phi) = 1 - M_0(\phi^2 - 1)^2$ with $0 < M_0 < 1$ is large in the bulk phases ($\phi = \pm 1$) but suppressed near the membrane, modeling a semi-permeable interface.

Remark 1. *Although the evolution equation (2.2) is written in Cahn–Hilliard form, the osmotic free energy in the present model contains no gradient term in ψ . As a result, the associated chemical potential $\nu = \delta F / \delta \psi$ contains no spatial derivatives, and the resulting Cahn–Hilliard equation is second order rather than fourth order. We retain the term “Cahn–Hilliard equation” to emphasize its conservative gradient-flow structure, consistent with related phase-field vesicle models.*

Free energy functional. The governing equations (2.1)–(2.2) are gradient flows of the total free energy

$$F[\phi, \psi] = F^{\text{surf}}[\phi] + F^{\text{bend}}[\phi] + F^{\text{area}}[\phi] + F^{\text{osm}}[\phi, \psi], \quad (2.3)$$

which combine surface, bending, arc-length, and osmotic contributions. The energy components are

$$F^{\text{surf}}[\phi] = \gamma_{\text{surf}} \int_{\Omega} f^{\text{surf}}(\phi, \nabla \phi) d\mathbf{x}, \quad (2.4)$$

$$F^{\text{bend}}[\phi] = \gamma_{\text{bend}} \int_{\Omega} f^{\text{bend}}(\phi, \Delta \phi) d\mathbf{x}, \quad (2.5)$$

$$F^{\text{osm}}[\phi, \psi] = \int_{\Omega} f^{\text{osm}}(\phi, \psi) d\mathbf{x}, \quad (2.6)$$

$$F^{\text{area}}[\phi] = \frac{\gamma_{\text{area}}}{2} \left(\int_{\Omega} f^{\text{surf}}(\phi, \nabla \phi) d\mathbf{x} - A \right)^2, \quad (2.7)$$

where γ_{surf} , γ_{bend} , and γ_{area} are surface tension, bending rigidity, and arc-length penalty coefficients, respectively.

The energy densities are [2, 5, 8]:

$$f^{\text{surf}}(\phi, \nabla \phi) = \frac{3\sqrt{2}}{4} \left(\frac{1}{\varepsilon} g(\phi) + \frac{\varepsilon}{2} |\nabla \phi|^2 \right), \quad (2.8a)$$

$$f^{\text{bend}}(\phi, \Delta \phi) = \frac{3\sqrt{2}}{16\varepsilon} \left(\frac{g'(\phi)}{\varepsilon} - \varepsilon \Delta \phi \right)^2, \quad (2.8b)$$

$$f^{\text{osm}}(\phi, \psi) = \frac{1+p(\phi)}{2} f^{\text{in}}(\psi) + \frac{1-p(\phi)}{2} f^{\text{out}}(\psi), \quad (2.8c)$$

where $g(\phi) = \frac{1}{4}(\phi^2 - 1)^2$ is the double-well potential, ε is the interface thickness, and

$$f^{\text{in/out}}(\psi) = \frac{\gamma_{\text{in/out}}}{2} (\psi - \psi_{\text{in/out}})^2 + \beta_{\text{in/out}}. \quad (2.9)$$

The osmotic energies are smoothly connected by an interpolation function $p(\phi)$ satisfying $p(1) = 1$, $p(-1) = -1$, and $p'(1) = p'(-1) = 0$. In all computations we take $p(\phi) = \sin\left(\frac{\pi}{2}\phi\right)$.

Chemical potentials and boundary conditions. With the energy functional defined, the chemical potentials are obtained as variational derivatives of $F[\phi, \psi]$. To circumvent the presence of explicit fourth-order derivatives in ϕ , an auxiliary variable $\omega := \frac{1}{\varepsilon}g'(\phi) - \varepsilon\Delta\phi$ is introduced. The resulting

expressions for the chemical potentials are

$$\begin{aligned}\mu &= \gamma_{\text{surf}} \frac{3\sqrt{2}}{4} \omega + \gamma_{\text{bend}} \frac{3\sqrt{2}}{8} \left(\frac{g''(\phi)}{\varepsilon^2} \omega - \Delta\omega \right) \\ &+ \gamma_{\text{area}} \left(\int_{\Omega} f^{\text{surf}}(\phi, \nabla\phi) \, d\mathbf{x} - A \right) \frac{3\sqrt{2}}{4} \omega + \frac{p'(\phi)}{2} (f^{\text{in}}(\psi) - f^{\text{out}}(\psi)),\end{aligned}\quad (2.10)$$

$$\nu = \frac{1 + p(\phi)}{2} \frac{df^{\text{in}}}{d\psi}(\psi) + \frac{1 - p(\phi)}{2} \frac{df^{\text{out}}}{d\psi}(\psi).\quad (2.11)$$

We impose homogeneous Neumann conditions $\partial_n\phi = \partial_n\mu = \partial_n\omega = \partial_n\psi = \partial_n\nu = 0$ on $\partial\Omega$.

Energy dissipation. The gradient-flow structure yields the energy dissipation law

$$\frac{dF}{dt} = - \int_{\Omega} (M_{\phi}|\mu|^2 + M_{\psi}(\phi)|\nabla\nu|^2) \, d\mathbf{x} \leq 0,\quad (2.12)$$

ensuring thermodynamic consistency.

2.2. MSAV Reformulation

We now introduce a reformulation based on the Multiple Scalar Auxiliary Variable (MSAV) method [4, 26]. Our goal is to preserve the thermodynamic structure of the original system while transforming the evolution equations into a form that leads to linear, decoupled, and energy-stable numerical schemes. The MSAV approach with multiple auxiliary variables is necessary because the disparate energy contributions, including the penalty terms for enforcing the arc-length constraint, behave very differently and cannot be properly handled with a single auxiliary variable [4].

Modified energy functional. Following the MSAV approach, the nonlinear contributions from the surface, bending, area, and osmotic energies are represented using scalar auxiliary variables $V(t)$, $U(t)$, $W(t)$, and $Z(t)$, respectively. The standard SAV framework introduces a linear stabilization parameter β in the energy splitting [26] to ensure sufficient dissipation in the implicit part of the scheme and to improve numerical stability when the nonlinear energy

dominates. We reformulate the bending energy through integration by parts.

$$\begin{aligned}
F^{\text{bend}}[\phi] &= \gamma_{\text{bend}} \int_{\Omega} \frac{3\sqrt{2}}{16\varepsilon} \left(\frac{g'(\phi)}{\varepsilon} - \varepsilon \Delta \phi \right)^2 d\mathbf{x} \\
&= \gamma_{\text{bend}} \int_{\Omega} \frac{3\sqrt{2}}{16\varepsilon} \left(\frac{1}{\varepsilon^2} (\phi^3 - \phi)^2 - 2|\nabla \phi|^2 + 6\phi^2|\nabla \phi|^2 + \varepsilon^2(\Delta \phi)^2 \right) d\mathbf{x}.
\end{aligned} \tag{2.13}$$

This decomposition reveals that the nonlinear terms $\frac{1}{\varepsilon^2}(\phi^3 - \phi)^2$ and $6\phi^2|\nabla \phi|^2$ are non-negative, satisfying the requirement that the nonlinear part of the energy be bounded from below—a key assumption of classical SAV-type methods. The modified total energy functional is then defined as

$$\begin{aligned}
E_{\text{mod}}(\phi, \psi; U, V, W, Z) &= \int_{\Omega} \left[\gamma_{\text{surf}} \frac{3\sqrt{2}}{4} \left(\frac{\varepsilon}{2} |\nabla \phi|^2 + \frac{\beta}{2\varepsilon} \phi^2 \right) \right] d\mathbf{x} \\
&\quad + \int_{\Omega} \left[\gamma_{\text{bend}} \frac{3\sqrt{2}}{16\varepsilon} (\varepsilon^2(\Delta \phi)^2 - 2|\nabla \phi|^2) \right] d\mathbf{x} \\
&\quad + \gamma_{\text{surf}} \frac{3\sqrt{2}}{4} V^2 + \frac{\gamma_{\text{area}}}{2} U^2 + \frac{3\sqrt{2}}{16\varepsilon} \gamma_{\text{bend}} W^2 \\
&\quad + \frac{1}{2} Z^2 - \gamma_{\text{surf}} \frac{3\sqrt{2}}{16\varepsilon} (\beta^2 + 2\beta),
\end{aligned} \tag{2.14}$$

where the constant ensures equivalence with the original energy functional. The auxiliary variables are defined by

$$V(t) = \sqrt{\int_{\Omega} \frac{(\phi^2 - 1 - \beta)^2}{4\varepsilon} d\mathbf{x}}, \quad W(t) = \sqrt{\int_{\Omega} \left(6\phi^2|\nabla \phi|^2 + \frac{(\phi^3 - \phi)^2}{\varepsilon^2} \right) d\mathbf{x}}, \tag{2.15a}$$

$$Z(t) = \sqrt{2 \int_{\Omega} f^{\text{osm}}(\phi, \psi) d\mathbf{x}}, \quad U(t) = \int_{\Omega} f^{\text{surf}}(\phi, \nabla \phi) d\mathbf{x} - A. \tag{2.15b}$$

Variational derivatives and reformulated equations. The variational derivatives of the nonlinear energy components are

$$S(\phi) = \frac{\frac{1}{\varepsilon}\phi(\phi^2 - 1 - \beta)}{2\sqrt{\int_{\Omega} \frac{1}{4\varepsilon}(\phi^2 - 1 - \beta)^2 d\mathbf{x}}}, \quad H(\phi) = \frac{3\sqrt{2}}{4} \left[\frac{1}{\varepsilon}\phi(\phi^2 - 1) - \varepsilon\Delta\phi \right], \quad (2.16)$$

$$Q(\phi) = \frac{6[\phi|\nabla\phi|^2 - \nabla \cdot (\phi^2\nabla\phi)] + \frac{1}{\varepsilon^2}(\phi^3 - \phi)(3\phi^2 - 1)}{\sqrt{\int_{\Omega} (6\phi^2|\nabla\phi|^2 + \frac{1}{\varepsilon^2}(\phi^3 - \phi)^2) d\mathbf{x}}}, \quad (2.17)$$

$$K(\phi, \psi) = \frac{p'(\phi)(f^{\text{in}}(\psi) - f^{\text{out}}(\psi))}{2\sqrt{\int_{\Omega} [(1 + p(\phi))f^{\text{in}}(\psi) + (1 - p(\phi))f^{\text{out}}(\psi)] d\mathbf{x}}}, \quad (2.18)$$

$$P(\phi, \psi) = \frac{\gamma_{\text{in}}(1 + p(\phi))(\psi - \psi_{\text{in}}) + \gamma_{\text{out}}(1 - p(\phi))(\psi - \psi_{\text{out}})}{2\sqrt{\int_{\Omega} [(1 + p(\phi))f^{\text{in}}(\psi) + (1 - p(\phi))f^{\text{out}}(\psi)] d\mathbf{x}}}. \quad (2.19)$$

The modified governing equations are

$$\frac{\partial\phi}{\partial t} = -M_{\phi}\mu, \quad (2.20)$$

$$\begin{aligned} \mu = & -\gamma_{\text{surf}} \frac{3\sqrt{2}\varepsilon}{4} \Delta\phi + \gamma_{\text{surf}} \frac{3\sqrt{2}\beta}{4\varepsilon} \phi + \gamma_{\text{bend}} \frac{3\sqrt{2}}{4\varepsilon} \Delta\phi + \gamma_{\text{bend}} \frac{3\sqrt{2}\varepsilon}{8} \Delta^2\phi \\ & + \gamma_{\text{surf}} \frac{3\sqrt{2}}{2} VS(\phi) + \gamma_{\text{area}} UH(\phi) + \gamma_{\text{bend}} \frac{3\sqrt{2}}{8\varepsilon} WQ(\phi) + ZK(\phi, \psi), \end{aligned} \quad (2.21)$$

$$\frac{\partial\psi}{\partial t} = \nabla \cdot (M_{\psi}(\phi)\nabla\nu), \quad (2.22)$$

$$\nu = ZP(\phi, \psi). \quad (2.23)$$

These equations preserve the gradient-flow structure while transforming nonlinear terms into linear couplings through the auxiliary variables. Homogeneous Neumann conditions are imposed:

$$\frac{\partial\phi}{\partial n} = \frac{\partial\mu}{\partial n} = \frac{\partial\psi}{\partial n} = \frac{\partial\nu}{\partial n} = 0 \quad \text{on } \partial\Omega. \quad (2.24)$$

Auxiliary variable evolution and initial conditions. Differentiating the auxiliary-variable definitions (2.15) in time and applying the chain rule yields

$$\frac{dV}{dt} = \int_{\Omega} S(\phi) \frac{\partial \phi}{\partial t} d\mathbf{x}, \quad \frac{dU}{dt} = \int_{\Omega} H(\phi) \frac{\partial \phi}{\partial t} d\mathbf{x}, \quad (2.25a)$$

$$\frac{dW}{dt} = \int_{\Omega} Q(\phi) \frac{\partial \phi}{\partial t} d\mathbf{x}, \quad \frac{dZ}{dt} = \int_{\Omega} \left[K(\phi, \psi) \frac{\partial \phi}{\partial t} + P(\phi, \psi) \frac{\partial \psi}{\partial t} \right] d\mathbf{x}. \quad (2.25b)$$

Initial conditions are

$$\begin{aligned} \phi|_{t=0} &= \phi^0, & \psi|_{t=0} &= \psi^0, & V|_{t=0} &= V(\phi^0), \\ U|_{t=0} &= U(\phi^0), & W|_{t=0} &= W(\phi^0), & Z|_{t=0} &= Z(\phi^0, \psi^0). \end{aligned} \quad (2.26)$$

Energy dissipation of the reformulated system. The reformulated system (2.20)–(2.25) with boundary conditions (2.24) and initial conditions (2.26) is equivalent to the original system (2.1)–(2.2) and preserves the thermodynamic structure. By taking the L^2 inner product of (2.20) with μ , of (2.21) with $\partial\phi/\partial t$, of (2.22) with ν , of (2.23) with $\partial\psi/\partial t$, and of (2.25) with V , U , W , and Z respectively, and then integrating by parts and summing all resulting equalities, we obtain

$$\frac{dE_{\text{mod}}}{dt} = - \int_{\Omega} M_{\phi} |\mu|^2 d\mathbf{x} - \int_{\Omega} M_{\psi}(\phi) |\nabla \nu|^2 d\mathbf{x} \leq 0. \quad (2.27)$$

Since $M_{\phi}, M_{\psi} > 0$, the modified energy decreases monotonically, preserving thermodynamic consistency.

3. Numerical Scheme Development

In this section, we develop a numerical scheme for the reformulated governing equations that achieves three main objectives: unconditional energy stability, mass conservation, and computational efficiency through constant-coefficient linear systems. The key innovation is a strategic reformulation of the stabilized MSAV approach that places Cahn–Hilliard stabilization directly in the evolution equation rather than in the chemical potential. This seemingly minor modification has profound computational consequences: all resulting elliptic systems possess constant coefficients despite the presence of variable mobility, enabling solution via fast transform methods rather than iterative solvers.

3.1. Overview of the Numerical Approach

Our scheme integrates three components to work together:

1. *Unconditional energy stability*: Rigorous discrete energy dissipation without time step restrictions (Theorems 3.1 and 3.2).
2. *Exact mass conservation*: Preserved at the discrete level through summation-by-parts identities.
3. *Computational efficiency*: Seven constant-coefficient elliptic systems per time step, solved directly via discrete cosine transforms.

Sections 3.2–3.4 detail the discretization and prove stability; Section 3.5 analyzes the computational structure and demonstrates performance gains.

3.2. Temporal Discretization and Stabilization Strategy

The system is discretized in time using a semi-implicit, second-order backward differentiation formula (BDF2). The scheme is based on the MSAV formulation from [4], where the nonlinear energy terms handled by the auxiliary variables are treated explicitly using second-order extrapolation.

Stabilization Strategy. A key feature of our approach is the introduction of linear stabilization terms to ensure robust performance for this stiff, coupled system. We consider two stabilization terms:

- *Allen–Cahn stabilization* ($\theta > 0$): A standard term $\theta(\Delta\phi^{*,n+1} - \Delta\phi^{n+1})$ in the chemical potential.
- *Cahn–Hilliard stabilization* ($\lambda > 0$): A novel term $\lambda(\Delta\psi^{n+1} - \Delta\psi^{*,n+1})$ placed directly in the evolution equation rather than in the chemical potential.

This strategic placement of the Cahn–Hilliard stabilization is crucial: while conventional approaches add stabilization inside the chemical potential [3], this leads to linear systems with variable coefficients due to the variable mobility $M_\psi(\phi)$. Our placement ensures that all resulting linear systems have constant coefficients, enabling the use of highly efficient fast direct solvers.

Main Time-Stepping Scheme (CC-MSAV-BDF2). Given solutions (ϕ^n, ψ^n) and (ϕ^{n-1}, ψ^{n-1}) at time levels n and $n-1$, we solve for the next time level (ϕ^{n+1}, ψ^{n+1}) via the following system:

$$\frac{3\phi^{n+1} - 4\phi^n + \phi^{n-1}}{2\Delta t} = -M_\phi \mu^{n+1}, \quad (3.1)$$

$$\begin{aligned} \mu^{n+1} = & -\gamma_{\text{surf}} \frac{3\sqrt{2}\varepsilon}{4} \Delta\phi^{n+1} + \theta(\Delta\phi^{*,n+1} - \Delta\phi^{n+1}) \\ & + \gamma_{\text{surf}} \frac{3\sqrt{2}\beta}{4\varepsilon} \phi^{n+1} + \gamma_{\text{bend}} \frac{3\sqrt{2}}{4\varepsilon} \Delta\phi^{*,n+1} \\ & + \gamma_{\text{bend}} \frac{3\sqrt{2}\varepsilon}{8} \Delta^2\phi^{n+1} + \gamma_{\text{surf}} \frac{3\sqrt{2}}{2} V^{n+1} S(\phi^{*,n+1}) \\ & + \gamma_{\text{area}} U^{n+1} H(\phi^{*,n+1}) + \gamma_{\text{bend}} \frac{3\sqrt{2}}{8\varepsilon} W^{n+1} Q(\phi^{*,n+1}) \\ & + Z^{n+1} K(\phi^{*,n+1}, \psi^{*,n+1}), \end{aligned} \quad (3.2)$$

$$\frac{3\psi^{n+1} - 4\psi^n + \psi^{n-1}}{2\Delta t} = \lambda(\Delta\psi^{n+1} - \Delta\psi^{*,n+1}) + \nabla \cdot (M_\psi(\phi^{*,n+1}) \nabla \nu^{n+1}), \quad (3.3)$$

$$\nu^{n+1} = Z^{n+1} P(\phi^{*,n+1}, \psi^{*,n+1}), \quad (3.4)$$

Scalar auxiliary variable updates:

$$3V^{n+1} - 4V^n + V^{n-1} = \int_{\Omega} S(\phi^{*,n+1}) (3\phi^{n+1} - 4\phi^n + \phi^{n-1}) d\mathbf{x}, \quad (3.5)$$

$$3U^{n+1} - 4U^n + U^{n-1} = \int_{\Omega} H(\phi^{*,n+1}) (3\phi^{n+1} - 4\phi^n + \phi^{n-1}) d\mathbf{x}, \quad (3.6)$$

$$3W^{n+1} - 4W^n + W^{n-1} = \int_{\Omega} Q(\phi^{*,n+1}) (3\phi^{n+1} - 4\phi^n + \phi^{n-1}) d\mathbf{x}, \quad (3.7)$$

$$\begin{aligned} 3Z^{n+1} - 4Z^n + Z^{n-1} = & \int_{\Omega} K(\phi^{*,n+1}, \psi^{*,n+1}) (3\phi^{n+1} - 4\phi^n + \phi^{n-1}) d\mathbf{x} \\ & + \int_{\Omega} P(\phi^{*,n+1}, \psi^{*,n+1}) (3\psi^{n+1} - 4\psi^n + \psi^{n-1}) d\mathbf{x}, \end{aligned} \quad (3.8)$$

where the second-order extrapolations are defined as

$$\phi^{*,n+1} = 2\phi^n - \phi^{n-1}, \quad \psi^{*,n+1} = 2\psi^n - \psi^{n-1}. \quad (3.9)$$

Remark 2 (Selection of stabilization parameters). *The stabilization parameters θ and λ are chosen to ensure physical energy stability and robust performance. Through systematic testing at $\varepsilon = 0.03125$ and $N = 256$, we adopt $\theta = 1.5$ for standard simulations (increased to $\theta = 30$ for challenging cases involving aggressive morphological changes) and $\lambda = 10^5$ for all cases, especially when the osmotic energy dominates. The detailed parameter selection procedure is provided in Appendix E.*

3.3. Energy Stability Analysis

A central advantage of the MSAV framework is its ability to produce schemes that satisfy discrete energy dissipation laws, thereby inheriting the thermodynamic structure of the continuous phase-field model. For our coupled Allen–Cahn–Cahn–Hilliard system with stabilization, we establish rigorous energy stability results that depend on the stabilization parameter λ .

The Modified Discrete Energy. The BDF2-MSAV framework requires a modified energy functional that accounts for both the multistep structure and the auxiliary variable formulation. For the standard MSAV approach applied to gradient flows, this modification is well-established [4]. However, our strategic placement of Cahn–Hilliard stabilization (Section 3.2) introduces a novel coupling structure that necessitates careful treatment.

The modified discrete energy at time level $n + 1$ takes the form

$$E_{\text{mod}}^{n+1,n} = E_{\text{BDF2}}^{n+1,n} - E_{\lambda}^{n+1}, \quad (3.10)$$

where:

- $E_{\text{BDF2}}^{n+1,n}$ captures the phase-field, auxiliary variable, and stabilization parameter θ contributions at t^{n+1} ,
- E_{λ}^{n+1} accumulates the weighted stabilization dissipation related to λ since the second time step.

Explicitly, the modified energy is given by

$$\begin{aligned}
E_{\text{mod}}^{n+1,n} = & \frac{1}{2} \gamma_{\text{bend}} \frac{3\sqrt{2}\varepsilon}{8} (\|\Delta\phi^{n+1}\|^2 + \|2\Delta\phi^{n+1} - \Delta\phi^n\|^2) \\
& + \frac{1}{2} \left(\gamma_{\text{surf}} \frac{3\sqrt{2}\varepsilon}{4} + \theta \right) (\|\nabla\phi^{n+1}\|^2 + \|2\nabla\phi^{n+1} - \nabla\phi^n\|^2) \\
& - \frac{1}{2} \tilde{\theta} (\|\nabla\phi^{n+1}\|^2 + \|2\nabla\phi^{n+1} - \nabla\phi^n\|^2 - 2\|\nabla\phi^{n+1} - \nabla\phi^n\|^2) \\
& + \frac{1}{2} \gamma_{\text{surf}} \frac{3\sqrt{2}\beta}{4\varepsilon} (\|\phi^{n+1}\|^2 + \|2\phi^{n+1} - \phi^n\|^2) \\
& + \frac{1}{2} \gamma_{\text{surf}} \frac{3\sqrt{2}}{2} ((V^{n+1})^2 + (2V^{n+1} - V^n)^2) \\
& + \frac{1}{2} \gamma_{\text{area}} ((U^{n+1})^2 + (2U^{n+1} - U^n)^2) \\
& + \frac{1}{2} \gamma_{\text{bend}} \frac{3\sqrt{2}}{8\varepsilon} ((W^{n+1})^2 + (2W^{n+1} - W^n)^2) \\
& + \frac{1}{2} ((Z^{n+1})^2 + (2Z^{n+1} - Z^n)^2) \\
& - \sum_{j=2}^{n+1} \frac{\Delta t}{2} \|d^j\|^2,
\end{aligned} \tag{3.11}$$

where $\tilde{\theta} = \theta + \gamma_{\text{bend}} \frac{3\sqrt{2}}{4\varepsilon}$ accounts for the extrapolation terms in the SAV framework, and $d^{n+1} = \frac{\lambda(\nabla\psi^{n+1} - \nabla\psi^{*,n+1})}{\sqrt{M_\psi(\phi^{*,n+1})}}$.

Theorem 3.1 (Unconditional Energy Stability). *Consider the numerical scheme (3.1)–(3.8) with the modified discrete energy represents the stabilization correction. Then the following stability property holds for all $n \geq 2$:*

$$\frac{E_{\text{mod}}^{n+1,n} - E_{\text{mod}}^{n,n-1}}{2\Delta t} + \frac{K^n}{2\Delta t} = - \left[M_\phi \|\mu^{n+1}\|^2 + \|c^{n+1} + \frac{1}{2}d^{n+1}\|^2 \right] \leq 0, \tag{3.12}$$

where $K^n \geq 0$ represents accumulated numerical dissipation arising from the BDF2 second-order differences $\|a^{n+1} - 2a^n + a^{n-1}\|^2$ across all discrete variables that are not scaled by λ (see Appendix A for the explicit expression), and

$$c^{n+1} = \sqrt{M_\psi(\phi^{*,n+1})} \nabla \nu^{n+1} \tag{3.13}$$

denotes the weighted gradient of the Cahn–Hilliard chemical potential.

Proof. The detailed proof is provided in Appendix A. \square

Remark 3 (Unconditional energy stability). *Inequality (3.12) holds without restriction on Δt , θ , or λ . Unlike standard MSAV schemes where stabilization enters through the chemical potential, we add it directly to the Cahn–Hilliard evolution equation, yielding (with variable mobility) the coupled dissipation $\|c^{n+1} + \frac{1}{2}d^{n+1}\|^2$. See Appendix A for details.*

3.4. Spatial Discretization

We employ the cell-centered finite difference framework on staggered grids developed by Wise [35]. This discretization is chosen for its *structure-preserving* properties, which are essential for transferring the continuous energy dissipation and mass conservation laws to the fully discrete level.

In particular, the scheme satisfies:

1. *Discrete summation-by-parts (SBP):* exact discrete analogs of integration by parts, enabling rigorous energy estimates without consistency errors;
2. *Exact mass conservation:* the conservative divergence structure ensures $\int_{\Omega} \phi^{n+1} dx = \int_{\Omega} \phi^n dx$ to machine precision at every time step.

The spatial domain $\Omega = (0, L_x) \times (0, L_y)$ is discretized using a uniform staggered grid with spacing h . Scalar variables (e.g., ϕ, ψ) are defined at cell centers, while fluxes are located on cell faces. Homogeneous Neumann boundary conditions are enforced through ghost cells. Complete definitions of the grid, discrete operators, inner products, and SBP identities are provided in Appendix D.

3.4.1. Structure-Preserving Discretization of Nonlinear Terms

While linear operators follow standard staggered-grid constructions, special care is required for nonlinear terms to preserve the continuous energy structure. All nonlinear operators are discretized in conservative form so that discrete SBP identities hold. We highlight the key ingredients below.

Quadratic face-averaging for cubic nonlinearities. To preserve exact discrete integration-by-parts for energy terms involving ϕ^3 , we employ a quadratic face-averaging operator. For east–west faces,

$$A_x^{(q)}(\phi^2)_{i+\frac{1}{2},j} = \frac{1}{3}(\phi_{i+1,j}^2 + \phi_{i+1,j}\phi_{i,j} + \phi_{i,j}^2), \quad (3.14)$$

with an analogous definition in the y -direction.

This averaging preserves the discrete product rule

$$D_x(\phi^3) = 3A_x^{(q)}(\phi^2) D_x\phi,$$

which yields the exact discrete identity

$$\mathbf{I}_h(\phi^3 \Delta_h \phi) = -3 \mathbf{I}_h(\phi^2 |\nabla_h \phi|^2), \quad (3.15)$$

fully consistent with the continuous gradient-flow structure.

Variable mobility flux. The Cahn–Hilliard flux with variable mobility is discretized conservatively as

$$[\nabla \cdot (M_\psi \nabla \nu)]_{i,j} = d_x(M_\psi(A_x \phi) D_x \nu)_{i,j} + d_y(M_\psi(A_y \phi) D_y \nu)_{i,j}, \quad (3.16)$$

where the mobility is evaluated at face centers via arithmetic averaging.

Nonlocal bending term. The nonlocal bending contribution $\phi |\nabla \phi|^2 - \nabla \cdot (\phi^2 \nabla \phi)$ requires a compatible discretization of both terms. We define

$$[\phi |\nabla \phi|^2]_{i,j} = \phi_{i,j} \left[\frac{|D_x \phi|_{i+\frac{1}{2},j}^2 + |D_x \phi|_{i-\frac{1}{2},j}^2}{2} + \frac{|D_y \phi|_{i,j+\frac{1}{2}}^2 + |D_y \phi|_{i,j-\frac{1}{2}}^2}{2} \right], \quad (3.17)$$

$$[\nabla \cdot (\phi^2 \nabla \phi)]_{i,j} = d_x((A_x \phi^2) D_x \phi)_{i,j} + d_y((A_y \phi^2) D_y \phi)_{i,j}. \quad (3.18)$$

This conservative formulation preserves the discrete SBP structure and yields an exact discrete bending-energy identity (see Appendix D for verification).

3.4.2. Fully-Discrete Energy Stability

The structure-preserving spatial discretization enables a direct extension of the semi-discrete energy stability result to the fully discrete scheme.

Theorem 3.2 (Fully-Discrete Energy Stability). *Let $E_h^{n+1,n}$ denote the fully discrete modified energy obtained from (3.11) by replacing all continuous operators and norms with their discrete counterparts defined in Appendix D. Then, for all $\Delta t > 0$ and $h > 0$,*

$$\frac{E_h^{n+1,n} - E_h^{n,n-1}}{2\Delta t} \leq - \left[M_\phi \|\mu_h^{n+1}\|_2^2 + \|c_h^{n+1} + \frac{1}{2}d_h^{n+1}\|_2^2 \right] \leq 0. \quad (3.19)$$

Proof. The proof follows identically to Theorem 3.1, with continuous inner products replaced by their discrete analogs. Homogeneous Neumann boundary conditions ensure that all boundary terms vanish in the discrete SBP identities, and the discrete Green's identity $(\phi, \Delta_h \psi)_h = -\|\nabla_h \phi\|_2^2$ holds exactly. \square

Remark 4 (Mass conservation). *Discrete mass conservation follows directly from the conservative flux formulation (3.16). For any discrete flux field satisfying the boundary conditions,*

$$h^2 \sum_{i,j} [\nabla_h \cdot \mathbf{F}]_{i,j} = 0,$$

implying $\sum_{i,j} \psi_{i,j}^{n+1} = \sum_{i,j} \psi_{i,j}^n$. Numerical experiments in Section 4 confirm relative mass errors below 5×10^{-11} .

3.5. Computational Efficiency: Fast Direct Solution

A primary objective of this work is to improve the computational efficiency of phase-field vesicle simulations through constant-coefficient reformulation. The essential distinction between the proposed and classical MSAV approaches lies in the structure of the resulting linear systems: the classical formulation produces *variable-coefficient* elliptic equations in the Cahn–Hilliard subsystem due to spatially-varying mobility, while the proposed reformulation yields *constant-coefficient* elliptic operators for all linear subproblems. This structural property enables direct solution via discrete cosine transforms (DCT) without matrix assembly or iteration, in contrast to classical methods requiring either sparse direct solvers or preconditioned Krylov iterations.

To provide a controlled comparison isolating the algorithmic contribution, we compare both MSAV implementations in MATLAB R2025b using identical numerical infrastructure (built-in sparse direct solver and DCT functions). Each time step requires solving seven linear elliptic systems: five fourth-order equations from the Allen–Cahn subsystem and two second-order equations from the Cahn–Hilliard subsystem. For rectangular domains with homogeneous Neumann boundary conditions, the constant-coefficient structure of all seven operators admits efficient DCT-based solutions.

3.5.1. Solution Algorithm and Complexity

The solution procedure at each time step consists of four stages with distinct computational characteristics:

Stages 1, 3–4: Lower-order operations. Explicit extrapolations $\phi^{*,n+1} = 2\phi^n - \phi^{n-1}$ and $\psi^{*,n+1} = 2\psi^n - \psi^{n-1}$ (Stage 1), solution of a dense 5×5 algebraic system for scalar auxiliary variable coefficients (Stage 3), and reconstruction of updated fields as linear combinations (Stage 4) each require $O(N^2)$ operations and contribute negligibly to overall complexity.

Stage 2: Elliptic system solution (dominant cost). The implicit discretization yields constant-coefficient operators

$$\chi(\phi) = C_1 \phi - C_2 \Delta_h \phi + C_3 \Delta_h^2 \phi, \quad (3.20)$$

$$\zeta(\psi) = \left(\frac{3}{2\Delta t} - \lambda \Delta_h \right) \psi, \quad (3.21)$$

where $C_1, C_2, C_3 > 0$ depend on model parameters and Δ_h denotes the discrete Laplacian. The five fourth-order equations share operator (3.20), while the two second-order equations share operator (3.21). The DCT diagonalizes both operators, reducing each solve to pointwise division in transform space (see Appendix C for implementation details).

The natural partitioning into two operator groups enables *batched* DCT evaluation: right-hand sides sharing identical operators are stacked along a third array dimension and transformed simultaneously via MATLAB’s multidimensional DCT. This requires only two forward-inverse DCT pairs per time step (one per operator type) rather than individual transforms for each of the seven equations. Each DCT evaluation requires approximately $4N^2 \log_2 N$ floating-point operations, yielding dominant per-timestep complexity

$$\mathcal{C}_{\text{DCT}} = O(N^2 \log N),$$

with a modest constant factor reflecting the specific structure (seven elliptic solves grouped into two batched operations). Beyond asymptotic scaling, batching reduces function call overhead and improves cache efficiency, contributing to the observed performance gains in Section 3.5.3.

3.5.2. Baseline Methods

For comparison, we implement the classical MSAV formulation using two standard approaches for the variable-coefficient Cahn–Hilliard subsystem:

Sparse direct solver (Classical+Direct). Assemble one sparse variable-coefficient matrix per time step for two direct solves (via MATLAB’s backslash) of the

Cahn–Hilliard subsystem equations. Robust but exhibits steep computational and memory growth with grid refinement. We also tested reuse of sparse LDL factorizations for the two Cahn–Hilliard solves per time step; however, at large grid sizes, the factorization cost and memory traffic dominated, providing no net speedup. We therefore report results using MATLAB’s optimized sparse backslash, which delivered the best direct-solver performance in our tests.

DCT-preconditioned PCG (Classical+DCT-PCG). Matrix-free operator application with DCT-based Poisson preconditioner (spatial-average mobility), constructed once per time step for two PCG solves. Maintains mesh-independent iteration counts (12–13 iterations) without parameter tuning. Incomplete factorizations (ILU, IC) performed poorly and are excluded.

The Allen–Cahn subsystem yields constant-coefficient equations in all formulations, solved identically via DCT across all three implementations. Performance differences therefore isolate the Cahn–Hilliard subsystem treatment, where the proposed constant-coefficient reformulation enables direct DCT solution versus variable-coefficient equations requiring sparse direct or iterative solvers in classical methods.

While reference implementations using fully coupled nonlinear multigrid (NLMG) in `Fortran` exist in the literature, our MATLAB-based comparison with identical numerical infrastructure provides a controlled assessment of the algorithmic impact of the constant-coefficient reformulation.

3.5.3. Performance Results

Figure 1 demonstrates substantial efficiency gains from the constant-coefficient reformulation across grid sizes $N = 128$ to 4096. At $N = 4096$, the proposed CC-MSAV+DCT scheme achieves approximately $6.5 \times$ speedup over DCT-preconditioned PCG and $15 \times$ over sparse direct methods. Both formulations discretize the same continuous model and maintain second-order accuracy in time and space, unconditional energy stability, and produce nearly indistinguishable solutions. (cf. Section 4.3) This confirms that efficiency gains arise purely from algorithmic structure rather than accuracy trade-offs.

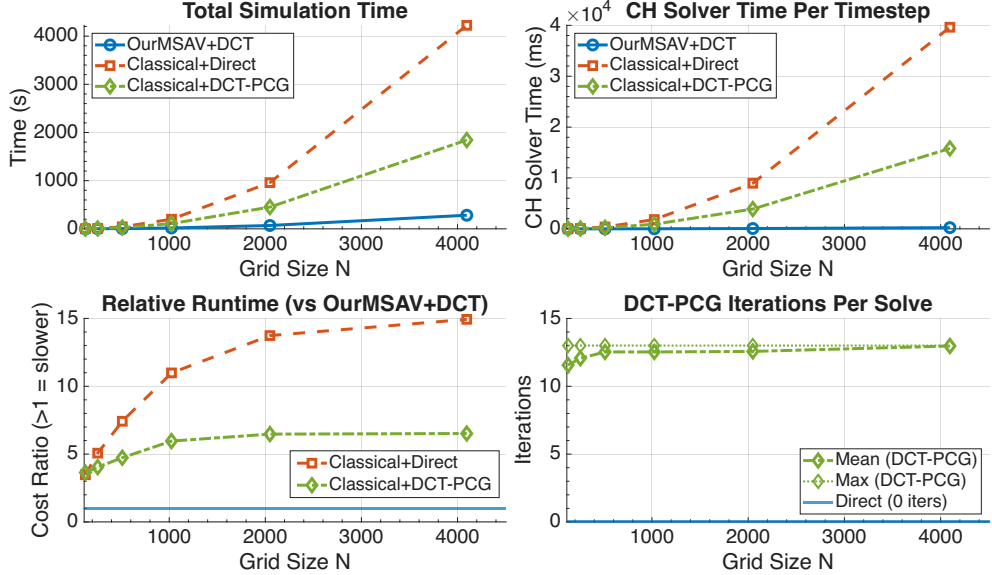


Figure 1: Runtime comparison for proposed CC-MSAV+DCT (blue) versus classical MSAV with sparse direct solver (red) and DCT-preconditioned PCG (green) on grids $N = 128\text{--}4096$. **(Top left)** Total simulation time for 100 time steps. **(Top right)** Per-timestep solver cost for Cahn–Hilliard subsystem. **(Bottom left)** Speedup factors showing $6\text{--}15\times$ acceleration at $N = 4096$. **(Bottom right)** PCG iteration counts (green diamonds) remain mesh-independent at 12–13 iterations; blue line marks zero iterations for direct DCT. All timings in MATLAB R2025b on identical hardware.

To further isolate the dominant computational bottleneck at the largest tested resolution, Table 1 reports the per-timestep Cahn–Hilliard solver cost and its fraction of total runtime at $N = 4096$.

Table 1: Cahn–Hilliard solver cost and overhead at $N = 4096$ (100 time steps).

Method	CH time per step (s)	CH fraction of total (%)	Relative CH speedup
CC-MSAV+DCT	0.237	8.4	1.0 \times
Classical+Direct	39.63	93.8	167 \times
Classical+DCT-PCG	15.80	85.7	67 \times

Scaling analysis. The key panels reveal distinct scaling behaviors:

- *Total runtime* (top left): The proposed method exhibits substantially milder growth with grid refinement compared to classical approaches. At $N = 4096$, 100 time steps require approximately 283 s for CC-MSAV+DCT versus 1844 s for Classical+DCT-PCG and 4224 s for Classical+Direct.

- *Per-timestep Cahn–Hilliard solver cost* (top right): This panel isolates the core algorithmic difference. At $N = 4096$, the per-timestep Cahn–Hilliard cost is 0.237 s for CC-MSAV+DCT, compared with 15.8 s for Classical+DCT-PCG ($\sim 67\times$ slower) and 39.6 s for Classical+Direct ($\sim 167\times$ slower). The Cahn–Hilliard subsystem dominates the runtime of classical formulations but accounts for less than 10% of the total cost in the proposed scheme.
- *Speedup factors* (bottom left): The advantage increases monotonically with grid refinement, from approximately $3\text{--}5\times$ at $N = 256$ to $6\text{--}15\times$ at $N = 4096$. This trend reflects the fundamental structural benefit of the proposed approach: classical methods require either repeated sparse matrix assembly or multiple Krylov iterations per time step, whereas the proposed scheme eliminates both through direct batched DCT solvers with $O(N^2 \log N)$ complexity.
- *Iteration counts* (bottom right): The DCT-based Poisson preconditioner maintains mesh-independent performance, requiring 12–13 PCG iterations per solve across all grid sizes. The proposed method requires zero iterations by design.

Practical implications. These efficiency gains enable several computational advantages for vesicle dynamics studies:

1. *High-resolution long-time simulations*: Resolutions $N \geq 2048$ become feasible for extended time integration, critical for capturing fine interfacial structures and long-time morphological evolution.
2. *Rapid parameter exploration*: Order-of-magnitude speedups facilitate systematic parameter sweeps, enabling more thorough investigation of model behavior across physically relevant regimes.
3. *Complex multi-vesicle systems*: Computational savings can be allocated to increased spatial detail or additional vesicles, expanding the scope of accessible biological scenarios.

The combination of unconditional energy stability, second-order accuracy, $O(N^2 \log N)$ complexity per time step, and low memory footprint (no assembled matrices) makes the proposed scheme particularly well-suited for large-scale computational investigations of biological membrane dynamics.

Limitations and scope. The constant-coefficient reformulation achieves maximum efficiency on rectangular domains with separable homogeneous boundary conditions, enabling fast transform solution via DCT (Neumann, as implemented), DST (Dirichlet), or FFT (periodic), all with $O(N^2 \log N)$ complexity. For irregular geometries or inhomogeneous boundary conditions, the method requires adaptation (e.g., domain embedding or preconditioned iterative solvers), potentially reducing but not eliminating the performance advantage. The fully decoupled structure remains advantageous for implementation simplicity and parallel scalability even when specialized iterative methods become competitive on complex geometries. The embarrassingly parallel structure of batched transform operations also suggests significant potential for GPU acceleration, which remains a subject for future investigation.

4. Numerical Results and Validation

In this section, we present numerical experiments demonstrating the accuracy and robustness of the proposed MSAV-based scheme. We begin by verifying the theoretical convergence rates through temporal, spatial, and coupled space–time studies (Section 4.1), then validating physical accuracy against the established NLMG benchmark (Section 4.2). Having confirmed correctness, we demonstrate that the constant-coefficient reformulation achieves significant computational efficiency without compromising accuracy (Section 4.3), and finally show solver robustness in geometrically complex single-vesicle scenarios (Section 4.4).

4.1. Convergence Studies

We verify the theoretical accuracy of the MSAV-BDF2 scheme through temporal and spatial convergence studies using the smooth elliptical initial condition from [29]. All parameters are listed in Table G.5 (Appendix G).

Temporal Convergence. Temporal convergence is measured using the Cauchy error method, comparing solutions at time steps Δt and $\Delta t/2$ at final time $T = 5 \times 10^{-3}$. We define the combined error for the coupled system as

$$\mathcal{E}_{\Delta t} = \sqrt{\|\phi^{\Delta t} - \phi^{\Delta t/2}\|_{L^2}^2 + \|\psi^{\Delta t} - \psi^{\Delta t/2}\|_{L^2}^2}, \quad (4.1)$$

with convergence rate $p = \log_2(\mathcal{E}_{\Delta t}/\mathcal{E}_{\Delta t/2})$. Tests use moderate stiffness $(\gamma_{\text{in}}, \gamma_{\text{out}}, \gamma_{\text{area}}) = (100, 100, 100)$ and osmotic equilibrium $\psi_{\text{in}} = 0.1$ on a fixed

512² grid. Table 2 shows second-order convergence with combined rates of 2.08–2.73 (average 2.40), confirming BDF2 accuracy.

Table 2: Temporal convergence rates for the coupled system at $T = 5 \times 10^{-3}$.

Δt	ϕ		ψ		Combined
	Error	Rate	Error	Rate	
1.0×10^{-5}	9.98×10^{-5}	—	1.26×10^{-2}	—	—
5.0×10^{-6}	1.26×10^{-5}	2.98	2.99×10^{-3}	2.08	2.08
2.5×10^{-6}	8.82×10^{-7}	3.84	4.52×10^{-4}	2.73	2.73
1.25×10^{-6}	7.81×10^{-8}	3.50	8.70×10^{-5}	2.38	2.38

Spatial Convergence. Spatial convergence is measured via numerical error between successive grid refinements $N \in \{128, 256, 512, 1024, 2048\}$ with fixed $\Delta t = 10^{-6}$ to ensure negligible temporal error. The error defined as $\mathcal{E}_h = \|u^h - \mathcal{I}(u^{h/2})\|_{L^2}$, where \mathcal{I} denotes cubic interpolation to the coarser grid. The combined error is defined analogously. Table 3 and Figure 2 demonstrate second-order spatial accuracy with asymptotic rate 2.00 for both fields and the coupled system.

Table 3: Spatial convergence rates at $T = 5 \times 10^{-3}$.

N	ϕ Error	Rate	ψ Error	Rate
128	3.7852×10^{-4}	—	3.0688×10^{-5}	—
256	9.5905×10^{-5}	1.98	7.7845×10^{-6}	1.98
512	2.4057×10^{-5}	2.00	1.9532×10^{-6}	1.99
1024	6.0191×10^{-6}	2.00	4.8875×10^{-7}	2.00

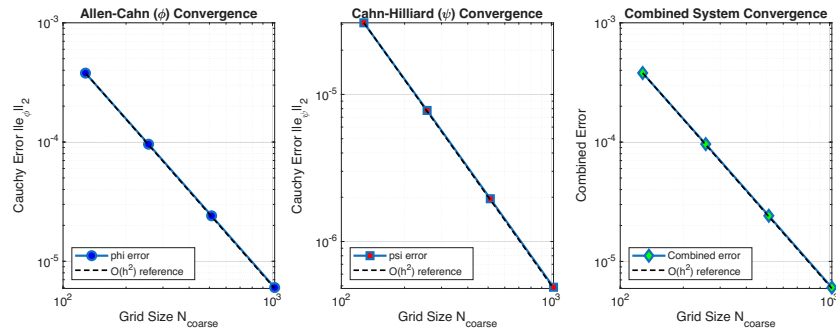


Figure 2: Spatial convergence for ϕ (left), ψ (middle), and combined system (right). Dashed lines show theoretical $O(h^2)$ rate.

Refinement-Path Convergence. To assess the overall convergence of the fully coupled scheme, we perform a refinement-path test where spatial and temporal resolutions are refined simultaneously according to $\Delta t = Ch$ with $C = 0.002$. The configuration parameters are listed in Table 4, with grid sizes from $N_0 = 128$ to $N_{\max} = 2048$ and final time $T = 5 \times 10^{-3}$. The error between successive refinement levels is defined as

$$\mathcal{E}_{h,\Delta t} = \sqrt{\|\phi^{(N)} - \mathcal{I}(\phi^{(2N)})\|_{L^2}^2 + \|\psi^{(N)} - \mathcal{I}(\psi^{(2N)})\|_{L^2}^2}, \quad (4.2)$$

where \mathcal{I} denotes cubic interpolation of the finer solution to the coarser grid.

Table 4 summarizes the coupled space–time convergence results. The scheme exhibits consistent second-order accuracy for both ϕ and ψ , with combined rates between 1.83 and 2.53 (average rate ≈ 2.2). These results confirm that the MSAV–BDF2 scheme maintains global second-order accuracy under simultaneous space–time refinement.

Table 4: Coupled space–time convergence results.

Level	N	Δt	$\ \mathcal{E}_\phi\ $	r_ϕ	$\ \mathcal{E}_\psi\ $	r_ψ	$\ \mathcal{E}_{\text{comb}}\ $	r_{comb}
1	128	1.563×10^{-5}	2.3757×10^{-3}	—	2.7560×10^{-2}	—	2.7662×10^{-2}	—
2	256	7.813×10^{-6}	5.8906×10^{-4}	2.012	5.2819×10^{-3}	2.383	5.3147×10^{-3}	2.381
3	512	3.906×10^{-6}	1.4080×10^{-4}	2.065	1.4821×10^{-3}	1.833	1.4887×10^{-3}	1.835
4	1024	1.953×10^{-6}	3.6117×10^{-5}	1.963	2.5566×10^{-4}	2.535	2.5820×10^{-4}	2.530

4.2. Benchmark Validation

We validate physical accuracy by comparing against the NLMG baseline solver [29] for canonical osmotic growth and shrinkage scenarios. Both tests use the same elliptical initial condition for ϕ^0 with distinct concentration profiles: $\psi^0 = -0.35\phi^0 + 0.45$ (growth) and $\psi^0 = -0.1\phi^0 + 0.7$ (shrinkage). All parameters follow Table G.5 with $\varepsilon = 0.03125$, $N = 256$, $\Delta t = 10^{-6}$, providing ~ 8 grid points per interface width.

Figures 3–4 demonstrate excellent agreement between both methods across all physical quantities: interface morphology, energy dissipation, arc length conservation, mass conservation, and concentration evolution. Both solvers correctly capture the multiphysics coupling and preserve thermodynamic consistency, validating the proposed MSAV scheme.

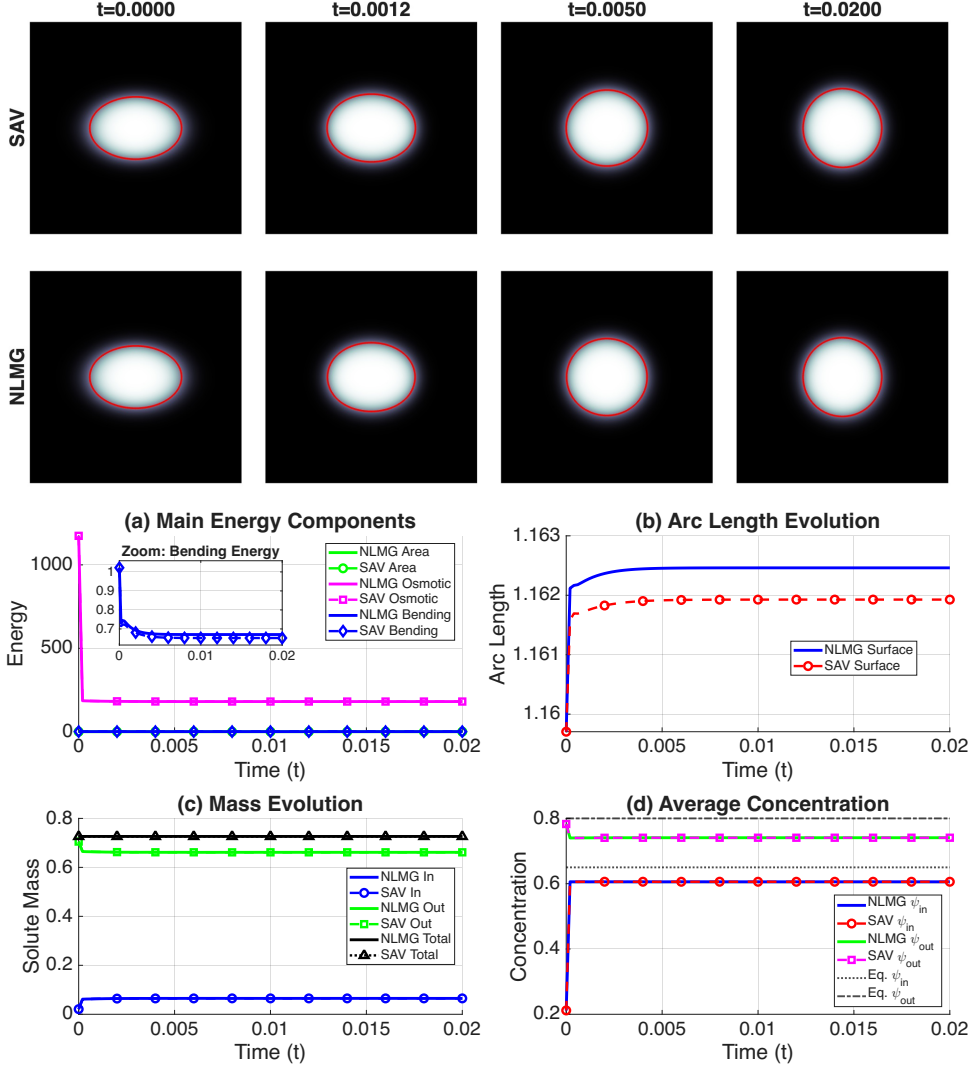


Figure 3: Elliptical growth validation. Top: Interface evolution (SAV: row 1; NLMG: row 2) at $t = 0, 0.005, 0.01, 0.02$. Bottom: Energy components, arc length, mass, and concentration dynamics. Excellent agreement validates physical accuracy.

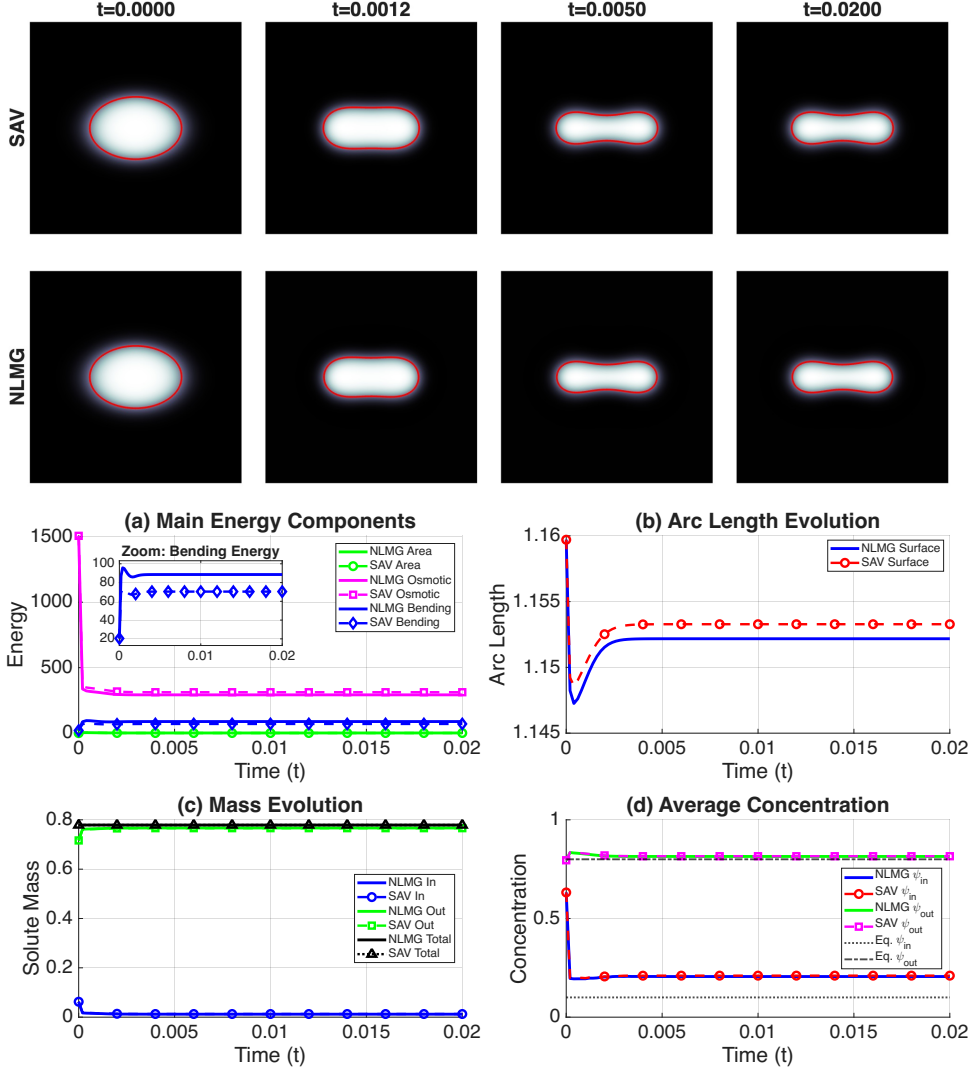


Figure 4: Elliptical shrinkage validation with $\gamma_{bend} = 1.0$ at $t = 0, 0.0012, 0.005, 0.02$. Top: Morphology (SAV: row 1; NLMG: row 2). Bottom: Quantitative comparison showing consistent dissipation, conservation, and dynamics.

4.3. Efficiency–Accuracy Validation

Having validated both convergence (Section 4.1) and physical accuracy (Section 4.2), we now examine whether the computational efficiency gains reported in Section 3.5 are obtained without any loss of accuracy. The validation is performed using the elliptical growth test described in Section 4.2.

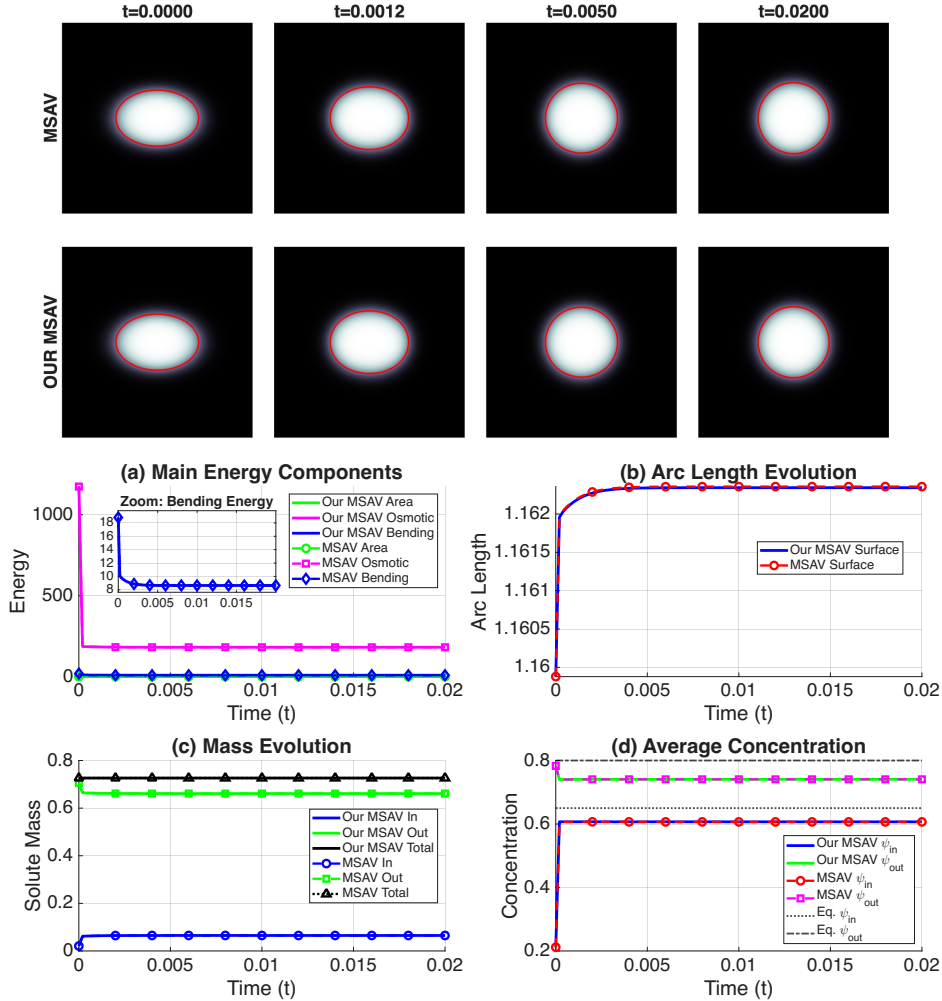


Figure 5: Accuracy comparison for the elliptical growth test. The first row corresponds to the classical MSAV method and the second row corresponds to the proposed CC-MSAV method. The top panels show the interface evolution at $t = 0, 0.0012, 0.005$, and 0.02 . The bottom panels contain the energy components and conservation metrics. The results remain visually and quantitatively indistinguishable, which confirms that the efficiency gains reported in Figure 1 are obtained without a reduction in accuracy.

4.4. Robustness to Complex Geometries and Large Deformations

Having validated accuracy and efficiency on smooth test problems (Sections 4.1–4.3), we now examine solver robustness under geometrically challenging conditions. A critical challenge for phase-field methods in vesicle dynamics is maintaining stability and conservation properties under large geometric deformations involving extreme morphologies. We evaluate the robustness of the proposed MSAV scheme through single-vesicle simulations with geometrically complex initial conditions that stress-test the method’s ability to handle sharp corners, concave regions, and high local curvature. All simulations employ a well-resolved diffuse-interface representation with $\varepsilon = 0.01$, $N = 2048$, $\Delta t = 5 \times 10^{-6}$, providing approximately twenty grid points across the interface. Non-elliptical initial shapes are smoothed using the procedure described in Appendix F. Unless otherwise specified, physical parameters follow Table G.5.

Growth dynamics. We first consider volume expansion under hypertonic conditions with parameters $(\gamma_{\text{bend}}, \theta) = (0.05, 10)$. Two distinct initial morphologies (triangle and star) are tested. As shown in Figure 6, both configurations undergo substantial rounding and evolve towards circular equilibrium configurations, consistent with energy minimization for expanding vesicles.

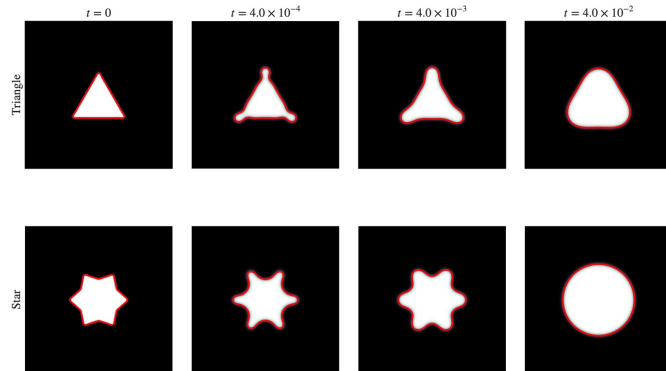


Figure 6: Single-vesicle growth under osmotic pressure ($\varepsilon = 0.01$, $N = 2048$). Both morphologies exhibit strong rounding and evolution towards circular equilibrium configurations.

Shrinkage dynamics. Shrinkage under hypotonic conditions $(\gamma_{\text{bend}}, \theta) = (0.1, 30)$ presents a more stringent test. Figure 7 demonstrates evolution

from four geometrically diverse initial shapes: triangle, incomplete hexagon, star, and crescent configurations, spanning a range of topological features, including sharp corners, concave regions, and varying aspect ratios.

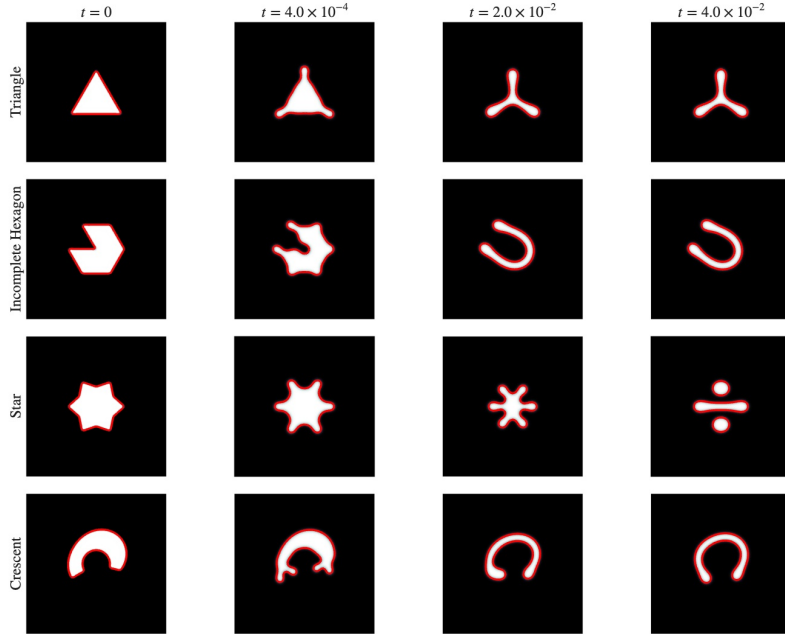


Figure 7: Single-vesicle shrinkage under osmotic pressure ($\varepsilon = 0.01$, $N = 2048$). Top: Four morphologies demonstrating solver robustness. Bottom: physical energy evolution showing steady dissipation, arc length conservation, and mass conservation for star and crescent configurations.

Detailed diagnostics for two representative cases (star and crescent) are shown in the lower panels of Figure 7. Physical energy decays steadily

toward steady states, with late-time convergence confirmed in the inset. Arc length deviations remain below 3.5% throughout evolution. Relative mass conservation errors remain within 5×10^{-11} , confirming excellent numerical conservation properties. All four morphologies exhibit similar conservation characteristics.

5. Conclusion and Future Work

We have developed an efficient, unconditionally energy-stable numerical scheme for simulating vesicle deformation under osmotic pressure using a phase-field approach. The method addresses a fundamental computational bottleneck in variable-mobility Cahn–Hilliard equations arising in vesicle models: achieving constant-coefficient linear systems without sacrificing unconditional stability.

Our key innovation is a reformulated stabilization strategy that incorporates the stabilization term directly into the evolution equation rather than the chemical potential. This yields fully decoupled constant-coefficient elliptic operators solvable via fast DCT in $O(N^2 \log N)$ operations. The resulting method eliminates the iterative solvers required by previous approaches, achieving 6–15× speedup on production grids ($N \geq 2048$) while maintaining second-order accuracy. Unconditional energy stability is rigorously established in Appendix A, where we prove that the modified energy functional decays monotonically without time step restrictions.

Comprehensive numerical experiments confirm the theoretical properties. The scheme exhibits second-order convergence in both space and time under successive refinement. Mass conservation is maintained to near-machine precision, with relative errors below 5×10^{-11} . Benchmark comparisons demonstrate close agreement with established nonlinear multigrid solvers for canonical growth and shrinkage scenarios. The modified energy decreases monotonically, as predicted by theory, while the physical energy exhibits steady dissipation in all test cases. The method handles complex geometries and non-convex initial shapes with topological changes robustly. Direct comparison between classical and constant-coefficient MSAV formulations confirms that efficiency gains come at no cost to accuracy.

Several directions for future work remain open. Coupling with Stokes equations would incorporate hydrodynamic effects in vesicle dynamics. Non-linear osmotic models could capture asymmetric responses observed in red blood cell pathologies such as sickle cell disease. The constant-coefficient

structure is well-suited for GPU acceleration and scalable parallel implementation, which would enable large-scale three-dimensional simulations. The combination of proven unconditional energy stability, second-order accuracy, optimal complexity scaling, and geometric flexibility makes the method particularly attractive for large-scale computational studies of biological membrane dynamics under osmotic stress.

Acknowledgments

SL acknowledges partial support from the National Science Foundation (NSF), Division of Mathematical Sciences, Grant DMS-2309798. SMW acknowledges the support from NSF, Division of Mathematical Sciences, Grant DMS-2309547. JL acknowledges partial support from NSF, Division of Mathematical Sciences, Grant DMS-2309800.

References

- [1] Elie Bretin, Luca Calatroni, and Simon Masnou. A mobility-sav approach for a cahn-hilliard equation with degenerate mobilities. *arXiv preprint arXiv:2306.15329*, 2023.
- [2] John W Cahn and John E Hilliard. Free energy of a nonuniform system. i. interfacial free energy. *The Journal of chemical physics*, 28(2):258–267, 1958.
- [3] Chuanjun Chen and Xiaofeng Yang. Fast, provably unconditionally energy stable, and second-order accurate algorithms for the anisotropic cahn–hilliard model. *Computer Methods in Applied Mechanics and Engineering*, 351:35–59, 2019.
- [4] Qing Cheng and Jie Shen. Multiple scalar auxiliary variable (msav) approach and its application to the phase-field vesicle membrane model. *SIAM Journal on Scientific Computing*, 40(6):A3982–A4006, 2018.
- [5] Qiang Du, Chun Liu, Rolf Ryham, and Xiaoqiang Wang. A phase field formulation of the willmore problem. *Nonlinearity*, 18(3):1249, 2005.
- [6] Qiang Du, Chun Liu, and Xiaoqiang Wang. A phase field approach in the numerical study of the elastic bending energy for vesicle membranes. *Journal of Computational Physics*, 198(2):450–468, 2004.

- [7] Yuval Elani, Robert V Law, and Oscar Ces. Vesicle-based artificial cells as chemical microreactors with spatially segregated reaction pathways. *Nature communications*, 5(1):5305, 2014.
- [8] Mi-Ho Giga, Arkadz Kirshtein, and Chun Liu. Variational modeling and complex fluids. *Handbook of mathematical analysis in mechanics of viscous fluids*, pages 1–41, 2017.
- [9] Ruihan Guo, Jie Shen, Shixin Xu, and Xianmin Xu. Phase-field modeling and energy-stable schemes for osmotic flow through semi-permeable. *arXiv preprint arXiv:2506.11374*, 2025.
- [10] Frank Haußer, S Li, J Lowengrub, W Marth, Andreas Rätz, and Axel Voigt. Thermodynamically consistent models for two-component vesicles. *Int. J. Biomath. Biostat.*, 2(1):19–48, 2013.
- [11] Qiong-Ao Huang, Wei Jiang, Jerry Zhijian Yang, and Cheng Yuan. A structure-preserving, upwind-sav scheme for the degenerate cahn–hilliard equation with applications to simulating surface diffusion. *Journal of Scientific Computing*, 97(3):64, 2023.
- [12] Yuen-Yick Kwan and Jie Shen. An efficient direct parallel spectral-element solver for separable elliptic problems. *Journal of Computational Physics*, 225(2):1721–1735, 2007.
- [13] Randall J LeVeque. *Finite difference methods for ordinary and partial differential equations: steady-state and time-dependent problems*. SIAM, 2007.
- [14] Kai Liu and Shuwang Li. Nonlinear simulations of vesicle wrinkling. *Mathematical Methods in the Applied Sciences*, 37(8):1093–1112, 2014.
- [15] Kai Liu, Gary R Marple, Jun Allard, Shuwang Li, Shravan Veerapaneni, and John Lowengrub. Dynamics of a multicomponent vesicle in shear flow. *Soft matter*, 13(19):3521–3531, 2017.
- [16] John S Lowengrub, Andreas Rätz, and Axel Voigt. Phase-field modeling of the dynamics of multicomponent vesicles: Spinodal decomposition, coarsening, budding, and fission. *Physical Review E—Statistical, Nonlinear, and Soft Matter Physics*, 79(3):031926, 2009.

- [17] Yoichiro Mori, Chun Liu, and Robert S Eisenberg. A model of electrodiffusion and osmotic water flow and its energetic structure. *Physica D: Nonlinear Phenomena*, 240(22):1835–1852, 2011.
- [18] Saulo Orizaga and Thomas Witelski. Imex methods for thin-film equations and cahn–hilliard equations with variable mobility. *Computational Materials Science*, 243:113145, 2024.
- [19] Bryan Quaife, Ashley Gannon, and Y-N Young. Hydrodynamics of a semipermeable inextensible membrane under flow and confinement. *Physical Review Fluids*, 6(7):073601, 2021.
- [20] Chaoyu Quan, Tao Tang, Boyi Wang, and Jiang Yang. A decreasing upper bound of energy for time-fractional phase-field equations. *arXiv preprint arXiv:2202.12192*, 2022.
- [21] David Salac and Michael Miksis. A level set projection model of lipid vesicles in general flows. *Journal of Computational Physics*, 230(22):8192–8215, 2011.
- [22] Ulrich Schumann and Roland A Sweet. Fast fourier transforms for direct solution of poisson’s equation with staggered boundary conditions. *Journal of Computational Physics*, 75(1):123–137, 1988.
- [23] Udo Seifert. Configurations of fluid membranes and vesicles. *Advances in physics*, 46(1):13–137, 1997.
- [24] ZHANG Senxiang, FENG Mei, and LUO Hong. Existence and regularity of the solution of the triplet phase separation equation. *Journal of Hainan University (Natural Science)*, 42(4):353–362, 2024.
- [25] Jie Shen. Efficient spectral-galerkin method i. direct solvers of second-and fourth-order equations using legendre polynomials. *SIAM Journal on Scientific Computing*, 15(6):1489–1505, 1994.
- [26] Jie Shen, Jie Xu, and Jiang Yang. The scalar auxiliary variable (sav) approach for gradient flows. *Journal of Computational Physics*, 353:407–416, 2018.
- [27] Jin Sun Sohn, Yu-Hau Tseng, Shuwang Li, Axel Voigt, and John S Lowengrub. Dynamics of multicomponent vesicles in a viscous fluid. *Journal of Computational Physics*, 229(1):119–144, 2010.

- [28] Gilbert Strang. The discrete cosine transform. *SIAM review*, 41(1):135–147, 1999.
- [29] Xiaoxia Tang, Shuwang Li, John S Lowengrub, and Steven M Wise. Phase field modeling and computation of vesicle growth or shrinkage. *Journal of mathematical biology*, 86(6):97, 2023.
- [30] Lloyd N Trefethen. *Spectral methods in MATLAB*. SIAM, 2000.
- [31] Shravan K Veerapaneni, Denis Gueyffier, George Biros, and Denis Zorin. A numerical method for simulating the dynamics of 3d axisymmetric vesicles suspended in viscous flows. *Journal of Computational Physics*, 228(19):7233–7249, 2009.
- [32] Shravan K Veerapaneni, Denis Gueyffier, Denis Zorin, and George Biros. A boundary integral method for simulating the dynamics of inextensible vesicles suspended in a viscous fluid in 2d. *Journal of Computational Physics*, 228(7):2334–2353, 2009.
- [33] CJ Vogl, MJ Miksis, SH Davis, and D Salac. The effect of glass-forming sugars on vesicle morphology and water distribution during drying. *Journal of The Royal Society Interface*, 11(99):20140646, 2014.
- [34] Xiaoqiang Wang and Qiang Du. Modelling and simulations of multi-component lipid membranes and open membranes via diffuse interface approaches. *Journal of mathematical biology*, 56(3):347–371, 2008.
- [35] Steven M Wise. Unconditionally stable finite difference, nonlinear multigrid simulation of the cahn-hilliard-hele-shaw system of equations. *Journal of Scientific Computing*, 44(1):38–68, 2010.
- [36] Wang Xiao, Kai Liu, John Lowengrub, Shuwang Li, and Meng Zhao. Three-dimensional numerical study on wrinkling of vesicles in elongation flow based on the immersed boundary method. *Physical Review E*, 107(3):035103, 2023.
- [37] Xiaofeng Yang, Jia Zhao, Qi Wang, and Jie Shen. Numerical approximations for a three-component cahn–hilliard phase-field model based on the invariant energy quadratization method. *Mathematical Models and Methods in Applied Sciences*, 27(11):1993–2030, 2017.

Appendix A. Complete Proof of Unconditional Energy Stability

This appendix provides the proof of Theorem 3.1. The overall proof methodology follows the standard MSAV-BDF2 framework established by Cheng and Shen [4]. We focus on the key novelty: the *Cahn–Hilliard stabilization* term $\lambda(\Delta\psi^{n+1} - \Delta\psi^{*,n+1})$ producing the remainder, and we absorb it as a difference between two accumulated sums. The coupled Allen–Cahn–Cahn–Hilliard structure with cross-phase coupling $K(\phi, \psi)$ and $P(\phi, \psi)$ is handled naturally within the MSAV framework through the auxiliary variable Z^{n+1} .

Appendix A.1. Notation and BDF2 Identities

Throughout, we use standard L^2 inner products (\cdot, \cdot) and norms $\|\cdot\|$. Extrapolated quantities at time level $n+1$ are denoted with superscript $*$, e.g., $M_\psi^* = M_\psi(\phi^{*,n+1}) > 0$, $K^* = K(\phi^{*,n+1}, \psi^{*,n+1})$, $P^* = P(\phi^{*,n+1}, \psi^{*,n+1})$. The proof relies on the following BDF2 identities [4]:

Lemma 1 (BDF2 Identities). *For any scalar or vector sequence $\{a^n\}$, the following identities hold:*

$$\begin{aligned} 2(3a^{n+1} - 4a^n + a^{n-1}, a^{n+1}) &= \|a^{n+1}\|^2 - \|a^n\|^2 \\ &\quad + \|2a^{n+1} - a^n\|^2 - \|2a^n - a^{n-1}\|^2 \\ &\quad + \|a^{n+1} - 2a^n + a^{n-1}\|^2, \end{aligned} \quad (\text{A.1})$$

$$\begin{aligned} 2(3a^{n+1} - 4a^n + a^{n-1}, 2a^n - a^{n-1}) &= \left(\|a^{n+1}\|^2 + \|2a^{n+1} - a^n\|^2 \right. \\ &\quad \left. - 2\|a^{n+1} - a^n\|^2 \right) \\ &\quad - \left(\|a^n\|^2 + \|2a^n - a^{n-1}\|^2 \right. \\ &\quad \left. - 2\|a^n - a^{n-1}\|^2 \right) \\ &\quad - 3\|a^{n+1} - 2a^n + a^{n-1}\|^2. \end{aligned} \quad (\text{A.2})$$

Appendix A.2. Weak Formulation and Completion of Squares

Taking the L^2 inner product of (3.1) with $2\Delta t \mu^{n+1}$ and (3.3) with $2\Delta t \nu^{n+1}$, and using integration by parts with homogeneous Neumann boundary conditions:

$$\begin{aligned} &(3\phi^{n+1} - 4\phi^n + \phi^{n-1}, \mu^{n+1}) + (3\psi^{n+1} - 4\psi^n + \psi^{n-1}, \nu^{n+1}) \\ &= -2\Delta t \left[M_\phi \|\mu^{n+1}\|^2 + (\nabla \nu^{n+1}, M_\psi^* \nabla \nu^{n+1}) + \lambda (\nabla \nu^{n+1}, \nabla \psi^{*,n+1} - \nabla \psi^{*,n+1}) \right]. \end{aligned} \quad (\text{A.3})$$

Handling the stabilization term. Define the auxiliary quantities:

$$c^{n+1} = \sqrt{M_\psi^*} \nabla \nu^{n+1}, \quad (\text{A.4})$$

$$d^{n+1} = \frac{\lambda(\nabla \psi^{n+1} - \nabla \psi^{*,n+1})}{\sqrt{M_\psi^*}}. \quad (\text{A.5})$$

Completing the square, the Cahn–Hilliard dissipation terms in (A.3) become:

$$\begin{aligned} & (\nabla \nu^{n+1}, M_\psi^* \nabla \nu^{n+1}) + \lambda(\nabla \nu^{n+1}, \nabla \psi^{n+1} - \nabla \psi^{*,n+1}) \\ &= \|c^{n+1}\|^2 + (c^{n+1}, d^{n+1}) = \|c^{n+1} + \frac{1}{2}d^{n+1}\|^2 - \frac{1}{4}\|d^{n+1}\|^2. \end{aligned} \quad (\text{A.6})$$

Thus (A.3) becomes:

$$\begin{aligned} & (3\phi^{n+1} - 4\phi^n + \phi^{n-1}, \mu^{n+1}) + (3\psi^{n+1} - 4\psi^n + \psi^{n-1}, \nu^{n+1}) \\ &= -2\Delta t \left[M_\phi \|\mu^{n+1}\|^2 + \|c^{n+1} + \frac{1}{2}d^{n+1}\|^2 \right] + \frac{\Delta t}{2} \|d^{n+1}\|^2. \end{aligned} \quad (\text{A.7})$$

Appendix A.3. Energy Decomposition

We expand the left-hand side of (A.7) by substituting the chemical potential definitions (3.2)–(3.4).

Appendix A.3.1. Standard Energy Terms

For all standard (implicitly treated) energy terms (surface, bending, area, and scalar auxiliary variables V, U, W), we apply integration by parts, followed by identities (A.1)–(A.2). Each contribution decomposes into:

- Energy differences between consecutive time levels: $\|a^{n+1}\|^2 - \|a^n\|^2 + \|2a^{n+1} - a^n\|^2 - \|2a^n - a^{n-1}\|^2$;
- Non-negative numerical dissipation: $\|a^{n+1} - 2a^n + a^{n-1}\|^2 \geq 0$,

where a represents $\Delta\phi, \nabla\phi, \phi$, or scalar auxiliary variables. The algebraic manipulations are identical to [4, Theorem 3.2].

Appendix A.3.2. Cross-Phase Coupling Through Auxiliary Variable Z

From the Allen–Cahn chemical potential (3.2), the coupling term K^* contributes:

$$(3\phi^{n+1} - 4\phi^n + \phi^{n-1}, Z^{n+1} K^*). \quad (\text{A.8})$$

From the Cahn–Hilliard side, the coupling term P^* contributes:

$$(3\psi^{n+1} - 4\psi^n + \psi^{n-1}, Z^{n+1}P^*). \quad (\text{A.9})$$

Combining (A.8)–(A.9) with the auxiliary variable evolution equation (3.8), we obtain:

$$\begin{aligned} & (3\phi^{n+1} - 4\phi^n + \phi^{n-1}, Z^{n+1}K^*) + (3\psi^{n+1} - 4\psi^n + \psi^{n-1}, Z^{n+1}P^*) \\ &= (3Z^{n+1} - 4Z^n + Z^{n-1}, Z^{n+1}). \end{aligned} \quad (\text{A.10})$$

Applying identity (A.1) with $a = Z$ to expand the right-hand side produces energy differences and numerical dissipation associated with the auxiliary variable Z .

Appendix A.3.3. Treatment of the Stabilization Remainder

The key novelty in our energy analysis is handling the positive remainder $\frac{\Delta t}{2} \|d^{n+1}\|^2$ that appears on the right-hand side of equation (A.7). Following the spirit of modified energy approaches for fractional equations [20], we rewrite this single-step contribution as a difference between two cumulative sums:

$$\frac{\Delta t}{2} \|d^{n+1}\|^2 = \left(\sum_{j=2}^{n+1} \frac{\Delta t}{2} \|d^j\|^2 \right) - \left(\sum_{j=2}^n \frac{\Delta t}{2} \|d^j\|^2 \right). \quad (\text{A.11})$$

Moving this telescoping difference to the left-hand side of (A.7) and incorporating it into the energy balance yields:

$$\begin{aligned} & (3\phi^{n+1} - 4\phi^n + \phi^{n-1}, \mu^{n+1}) + (3\psi^{n+1} - 4\psi^n + \psi^{n-1}, \nu^{n+1}) \\ & - \left(\sum_{j=2}^{n+1} \frac{\Delta t}{2} \|d^j\|^2 \right) + \left(\sum_{j=2}^n \frac{\Delta t}{2} \|d^j\|^2 \right) \\ &= -2\Delta t \left[M_\phi \|\mu^{n+1}\|^2 + \|c^{n+1} + \frac{1}{2}d^{n+1}\|^2 \right]. \end{aligned} \quad (\text{A.12})$$

The cumulative sum $-\sum_{j=2}^{n+1} \frac{\Delta t}{2} \|d^j\|^2$ now appears as part of the modified energy at time level $n+1$, while $-\sum_{j=2}^n \frac{\Delta t}{2} \|d^j\|^2$ appears in the energy at time level n . This structure ensures that the stabilization contribution accumulates properly across time steps while maintaining the overall energy dissipation property.

Appendix A.4. Assembly and Final Energy Balance

Collecting all contributions from the standard terms, cross-phase coupling, and stabilization, the left-hand side of (A.12) equals:

$$E_{\text{mod}}^{n+1,n} - E_{\text{mod}}^{n,n-1} + K^n, \quad (\text{A.13})$$

where $E_{\text{mod}}^{n+1,n}$ is the modified discrete energy (3.11), and K^n collects all non-negative numerical dissipation arising from the BDF2 second-order differences. Explicitly:

$$\begin{aligned} K^n = & \frac{1}{2} \gamma_{\text{bend}} \frac{3\sqrt{2}\varepsilon}{8} \|\Delta\phi^{n+1} - 2\Delta\phi^n + \Delta\phi^{n-1}\|^2 \\ & + \frac{1}{2} \left(\gamma_{\text{surf}} \frac{3\sqrt{2}\varepsilon}{4} + \theta \right) \|\nabla\phi^{n+1} - 2\nabla\phi^n + \nabla\phi^{n-1}\|^2 \\ & + \frac{3\tilde{\theta}}{2} \|\nabla\phi^{n+1} - 2\nabla\phi^n + \nabla\phi^{n-1}\|^2 \\ & + \frac{1}{2} \gamma_{\text{surf}} \frac{3\sqrt{2}\beta}{4\varepsilon} \|\phi^{n+1} - 2\phi^n + \phi^{n-1}\|^2 \\ & + \frac{1}{2} \gamma_{\text{surf}} \frac{3\sqrt{2}}{2} (V^{n+1} - 2V^n + V^{n-1})^2 \\ & + \frac{1}{2} \gamma_{\text{area}} (U^{n+1} - 2U^n + U^{n-1})^2 \\ & + \frac{1}{2} \gamma_{\text{bend}} \frac{3\sqrt{2}}{8\varepsilon} (W^{n+1} - 2W^n + W^{n-1})^2 \\ & + \frac{1}{2} (Z^{n+1} - 2Z^n + Z^{n-1})^2 \geq 0. \end{aligned} \quad (\text{A.14})$$

Combining (A.13) with (A.12) and dividing by $2\Delta t$:

$$\frac{E_{\text{mod}}^{n+1,n} - E_{\text{mod}}^{n,n-1}}{2\Delta t} + \frac{K^n}{2\Delta t} = - \left[M_\phi \|\mu^{n+1}\|^2 + \|c^{n+1} + \frac{1}{2}d^{n+1}\|^2 \right] \leq 0. \quad (\text{A.15})$$

This establishes the unconditional energy stability stated in Theorem 3.1. \square

Appendix B. Numerical Solution of the Fully Discretized System

In this section, we detail the procedure for solving the coupled linear systems arising from the fully discretized schemes. The core of our approach

is to efficiently reduce the large system for the field variables (ϕ^{n+1}, ψ^{n+1}) to a small, dense linear system for a few unknown scalar integrals. This strategy, common in SAV-based methods, avoids the need to solve a large, non-local system directly.

The procedure is nearly identical for both the second-order BDF2 and first-order BDF1 schemes. We present the derivation for the BDF2 case; the BDF1 case follows by substituting the BDF1 operators for their BDF2 counterparts.

Step 1: Expressing SAVs in Terms of Field Variables

First, we rearrange the discrete evolution equations for the SAVs (Equations (3.5)–(3.8)) to express the new SAVs $(V^{n+1}, U^{n+1}, W^{n+1}, Z^{n+1})$ as functions of known past values and unknown integrals involving the new field variables ϕ^{n+1} and ψ^{n+1} . For example, for V^{n+1} :

$$V^{n+1} = \frac{1}{3} \left(4V^n - V^{n-1} + \int_{\Omega} S(\phi^{*,n+1})(3\phi^{n+1} - 4\phi^n + \phi^{n-1}) d\mathbf{x} \right). \quad (\text{B.1})$$

Step 2: Rearrangement into Linear System Form

With the SAVs expressed in terms of the field variables, we substitute them back into the discretized Allen–Cahn and Cahn–Hilliard equations. This substitution results in a large, fully coupled system. The crucial task is to algebraically rearrange this system to isolate all terms involving the unknown fields at the new time step, ϕ^{n+1} and ψ^{n+1} .

Our strategy places all implicit terms on the left-hand side (LHS) and all explicit terms (i.e., terms from previous time steps n and $n - 1$) on the right-hand side (RHS). This process transforms the equations into a structure amenable to linear solution, which we detail in the subsequent steps. For clarity, we present the rearrangement for each governing equation separately.

Allen–Cahn Equation

After substitution and rearrangement, the Allen–Cahn equation takes the following form, where the LHS contains all operators acting on the unknown

fields ϕ^{n+1} and ψ^{n+1} :

$$\begin{aligned}
& \left\{ \frac{3}{2\Delta t} + M_\phi \gamma_{\text{surf}} \frac{3\sqrt{2}\beta}{4\varepsilon} \right. \\
& \quad \left. - M_\phi \left(\gamma_{\text{surf}} \frac{3\sqrt{2}\varepsilon}{4} + \theta \right) \Delta + M_\phi \gamma_{\text{bend}} \frac{3\sqrt{2}\varepsilon}{8} \Delta^2 \right\} \phi^{n+1} \\
& + M_\phi \gamma_{\text{surf}} \frac{3\sqrt{2}}{2} \left(\int_{\Omega} S(\phi^{*,n+1}) \phi^{n+1} d\mathbf{x} \right) S(\phi^{*,n+1}) \\
& + M_\phi \gamma_{\text{area}} \left(\int_{\Omega} H(\phi^{*,n+1}) \phi^{n+1} d\mathbf{x} \right) H(\phi^{*,n+1}) \\
& + M_\phi \gamma_{\text{bend}} \frac{3\sqrt{2}}{8\varepsilon} \left(\int_{\Omega} Q(\phi^{*,n+1}) \phi^{n+1} d\mathbf{x} \right) Q(\phi^{*,n+1}) \\
& + M_\phi \left(\int_{\Omega} K(\phi^{*,n+1}, \psi^{*,n+1}) \phi^{n+1} d\mathbf{x} \right) K(\phi^{*,n+1}, \psi^{*,n+1}) \\
& + M_\phi \left(\int_{\Omega} P(\phi^{*,n+1}, \psi^{*,n+1}) \psi^{n+1} d\mathbf{x} \right) K(\phi^{*,n+1}, \psi^{*,n+1}) = f^n. \quad (\text{B.2})
\end{aligned}$$

The RHS, denoted by f^n , consolidates all explicit terms:

$$\begin{aligned}
f^n = & \frac{4\phi^n - \phi^{n-1}}{2\Delta t} - M_\phi \left\{ \left(\theta + \gamma_{\text{bend}} \frac{3\sqrt{2}}{4\varepsilon} \right) \Delta \phi^{*,n+1} \right. \\
& + \gamma_{\text{surf}} \frac{3\sqrt{2}}{6} \left[4V^n - V^{n-1} + \int_{\Omega} S(\phi^{*,n+1}) (-4\phi^n + \phi^{n-1}) d\mathbf{x} \right] S(\phi^{*,n+1}) \\
& + \frac{\gamma_{\text{area}}}{3} \left[4U^n - U^{n-1} + \int_{\Omega} H(\phi^{*,n+1}) (-4\phi^n + \phi^{n-1}) d\mathbf{x} \right] H(\phi^{*,n+1}) \\
& + \gamma_{\text{bend}} \frac{3\sqrt{2}}{24\varepsilon} \left[4W^n - W^{n-1} + \int_{\Omega} Q(\phi^{*,n+1}) (-4\phi^n + \phi^{n-1}) d\mathbf{x} \right] \\
& \quad \times Q(\phi^{*,n+1}) \\
& + \frac{1}{3} \left[4Z^n - Z^{n-1} + \int_{\Omega} K(\phi^{*,n+1}, \psi^{*,n+1}) (-4\phi^n + \phi^{n-1}) d\mathbf{x} \right. \\
& \quad \left. + \int_{\Omega} P(\phi^{*,n+1}, \psi^{*,n+1}) (-4\psi^n + \psi^{n-1}) d\mathbf{x} \right] K(\phi^{*,n+1}, \psi^{*,n+1}) \left. \right\}. \quad (\text{B.3})
\end{aligned}$$

Cahn–Hilliard Equation

A similar procedure is applied to the Cahn–Hilliard equation. To maintain linearity, the phase-dependent mobility $M_\psi(\phi^{n+1})$ is treated semi-implicitly by evaluating it at $\phi^{*,n+1}$. The final rearranged form is

$$\begin{aligned} & \left(\frac{3}{2\Delta t} - \lambda\Delta \right) \psi^{n+1} \\ & - \left[\int_{\Omega} K(\phi^{*,n+1}, \psi^{*,n+1}) \phi^{n+1} d\mathbf{x} \right] \nabla \cdot (M_\psi(\phi^{*,n+1}) \nabla P(\phi^{*,n+1}, \psi^{*,n+1})) \\ & - \left[\int_{\Omega} P(\phi^{*,n+1}, \psi^{*,n+1}) \psi^{n+1} d\mathbf{x} \right] \nabla \cdot (M_\psi(\phi^{*,n+1}) \nabla P(\phi^{*,n+1}, \psi^{*,n+1})) \\ & = g^n. \end{aligned} \quad (\text{B.4})$$

The RHS, g^n , containing all explicit terms, is given by

$$g^n = \frac{4\psi^n - \psi^{n-1}}{2\Delta t} - \lambda\Delta\psi^{*,n+1} + \nabla \cdot (M_\psi(\phi^{*,n+1}) \nabla \tilde{\nu}^{n+1}), \quad (\text{B.5})$$

where $\tilde{\nu}^{n+1}$, the explicit portion of the chemical potential, is defined as

$$\begin{aligned} \tilde{\nu}^{n+1} = & \frac{1}{3} \left[4Z^n - Z^{n-1} + \int_{\Omega} K(\phi^{*,n+1}, \psi^{*,n+1}) (-4\phi^n + \phi^{n-1}) d\mathbf{x} \right. \\ & \left. + \int_{\Omega} P(\phi^{*,n+1}, \psi^{*,n+1}) (-4\psi^n + \psi^{n-1}) d\mathbf{x} \right] P(\phi^{*,n+1}, \psi^{*,n+1}). \end{aligned} \quad (\text{B.6})$$

This rearrangement successfully prepares the system for the decoupled solution procedure described next.

Step 3: Decoupling via Linear Operators

To solve the coupled system, we first decouple the spatial differential operators from the integral terms. This is achieved by defining two linear, constant-coefficient elliptic operators, χ and ζ , which collect all implicit linear terms for ϕ and ψ , respectively.

The operator for the Allen–Cahn equation, χ , is defined as

$$\chi(\phi) := C_{1,\chi}\phi - C_{2,\chi}\Delta\phi + C_{3,\chi}\Delta^2\phi, \quad (\text{B.7})$$

where

$$C_{1,\chi} = \frac{3}{2\Delta t} + M_\phi \gamma_{\text{surf}} \frac{3\sqrt{2}\beta}{4\varepsilon}, \quad (\text{B.8})$$

$$C_{2,\chi} = M_\phi \left[\gamma_{\text{surf}} \frac{3\sqrt{2}\varepsilon}{4} + \theta \right], \quad (\text{B.9})$$

$$C_{3,\chi} = M_\phi \gamma_{\text{bend}} \frac{3\sqrt{2}\varepsilon}{8}. \quad (\text{B.10})$$

The operator for the Cahn–Hilliard equation, ζ , is defined as

$$\zeta(\psi) := \left(\frac{3}{2\Delta t} - \lambda \Delta \right) \psi. \quad (\text{B.11})$$

Remark 5 (Well-posedness of Linear Operators). *The discrete operators χ and ζ are well-posed under the homogeneous Neumann boundary conditions implemented through ghost cells in the cell-centered finite difference framework.*

Given the expression $\chi(\phi) = C_{1,\chi}\phi - C_{2,\chi}\Delta_h\phi + C_{3,\chi}\Delta_h^2\phi$, we analyze the properties of the discrete Laplacian operator, Δ_h . For a system with Neumann boundary conditions, the eigenvalues $\lambda_{k,\ell}$ of Δ_h are given by:

$$\lambda_{k,\ell} = -\frac{4}{h^2} \left[\sin^2 \left(\frac{k\pi h}{2L_x} \right) + \sin^2 \left(\frac{\ell\pi h}{2L_y} \right) \right]$$

where the indices run from $k = 0, \dots, m-1$ and $\ell = 0, \dots, n-1$.

Note that these eigenvalues are non-positive (i.e., $-\lambda_{k,\ell} \geq 0$). The specific case $\lambda_{0,0} = 0$ corresponds to the constant mode. The spectrum of the discrete operator χ consists of eigenvalues:

$$\sigma_{k,\ell} = C_{1,\chi} - C_{2,\chi}\lambda_{k,\ell} + C_{3,\chi}\lambda_{k,\ell}^2.$$

For the constant mode ($k = \ell = 0$), we have $\sigma_{0,0} = C_{1,\chi} > 0$. For all other modes, since $-\lambda_{k,\ell} > 0$ and all coefficients are positive, we obtain

$$\sigma_{k,\ell} = C_{1,\chi} + C_{2,\chi}|\lambda_{k,\ell}| + C_{3,\chi}\lambda_{k,\ell}^2 > C_{1,\chi} > 0,$$

ensuring invertibility of the discrete system.

For $\zeta(\psi) = \frac{3}{2\Delta t}\psi - \lambda\Delta_h\psi$: This is a discrete Poisson-type operator. Using the same eigenvalues of Δ_h , the spectrum of ζ is:

$$\tau_{k,\ell} = \frac{3}{2\Delta t} - \lambda\lambda_{k,\ell} = \frac{3}{2\Delta t} + \lambda|\lambda_{k,\ell}| \geq \frac{3}{2\Delta t} > 0,$$

guaranteeing unique solvability. The strictly positive spectrum ensures that the discrete linear systems can be efficiently solved using fast direct methods such as the discrete cosine transform (DCT) for problems with Neumann boundary conditions.

Using these definitions, the fully discretized system can be formally rewritten. For brevity, we introduce the shorthand notation $S^* = S(\phi^{*,n+1})$, $H^* = H(\phi^{*,n+1})$, $Q^* = Q(\phi^{*,n+1})$, $K^* = K(\phi^{*,n+1}, \psi^{*,n+1})$, $P^* = P(\phi^{*,n+1}, \psi^{*,n+1})$, and the following scalar coefficients:

$$c_{gs} = M_\phi \gamma_{\text{surf}} \frac{3\sqrt{2}}{2}, \quad c_{ga} = M_\phi \gamma_{\text{area}}, \quad (\text{B.12})$$

$$c_{gb} = M_\phi \gamma_{\text{bend}} \frac{3\sqrt{2}}{8\varepsilon}, \quad c_{go} = M_\phi. \quad (\text{B.13})$$

The coupled Allen–Cahn–Cahn–Hilliard system can then be written as

$$\begin{aligned} \phi^{n+1} + c_{gs} \left[\int_{\Omega} S^* \phi^{n+1} d\mathbf{x} \right] \chi^{-1}(S^*) \\ + c_{ga} \left[\int_{\Omega} H^* \phi^{n+1} d\mathbf{x} \right] \chi^{-1}(H^*) \\ + c_{gb} \left[\int_{\Omega} Q^* \phi^{n+1} d\mathbf{x} \right] \chi^{-1}(Q^*) \\ + c_{go} \left[\int_{\Omega} K^* \phi^{n+1} d\mathbf{x} \right] \chi^{-1}(K^*) \\ + c_{go} \left[\int_{\Omega} P^* \psi^{n+1} d\mathbf{x} \right] \chi^{-1}(K^*) \\ = \chi^{-1}(f^n), \end{aligned} \quad (\text{B.14})$$

$$\begin{aligned} \psi^{n+1} - \left[\int_{\Omega} K^* \phi^{n+1} d\mathbf{x} \right] \zeta^{-1} (\nabla \cdot (M_\psi(\phi^{*,n+1}) \nabla P^*)) \\ - \left[\int_{\Omega} P^* \psi^{n+1} d\mathbf{x} \right] \zeta^{-1} (\nabla \cdot (M_\psi(\phi^{*,n+1}) \nabla P^*)) \\ = \zeta^{-1}(g^n). \end{aligned} \quad (\text{B.15})$$

Step 4: Derivation of the Small Linear System

The final step in the solution procedure is to solve for the unknown scalar integrals. This is achieved by reducing the large, coupled PDE system to a small, dense algebraic system.

First, we define the unknown integrals that appear in the expressions for ϕ^{n+1} and ψ^{n+1} :

$$\tilde{B} = \int_{\Omega} S(\phi^{*,n+1})\phi^{n+1} d\mathbf{x}, \quad \tilde{C} = \int_{\Omega} H(\phi^{*,n+1})\phi^{n+1} d\mathbf{x}, \quad (\text{B.16})$$

$$\tilde{D} = \int_{\Omega} Q(\phi^{*,n+1})\phi^{n+1} d\mathbf{x}, \quad \tilde{E} = \int_{\Omega} K(\phi^{*,n+1}, \psi^{*,n+1})\phi^{n+1} d\mathbf{x}, \quad (\text{B.17})$$

$$\tilde{G} = \int_{\Omega} P(\phi^{*,n+1}, \psi^{*,n+1})\psi^{n+1} d\mathbf{x}. \quad (\text{B.18})$$

By taking the inner product of the formally solved Allen–Cahn and Cahn–Hilliard equations (Equations (B.14)–(B.15)) with each of the relevant basis functions, we obtain a coupled 5×5 linear system for the unknowns $\tilde{B}, \tilde{C}, \tilde{D}, \tilde{E}, \tilde{G}$. This system is written in compact matrix form:

$$\mathbf{M}_{\phi,\psi} \begin{pmatrix} \tilde{B} \\ \tilde{C} \\ \tilde{D} \\ \tilde{E} \\ \tilde{G} \end{pmatrix} = \mathbf{b}_{\phi,\psi}. \quad (\text{B.19})$$

To express the matrix and vector compactly, we use the inner product notation $(f, g) = \int_{\Omega} fg d\mathbf{x}$ and define $\hat{S}^* = \chi^{-1}(S^*)$, $\hat{H}^* = \chi^{-1}(H^*)$, $\hat{Q}^* = \chi^{-1}(Q^*)$, and $\hat{K}^* = \chi^{-1}(K^*)$. Additionally, we introduce $\Lambda_{P^*} = \zeta^{-1}(\nabla \cdot (M_{\psi}(\phi^{*,n+1})\nabla P^*))$.

The right-hand side vector $\mathbf{b}_{\phi,\psi}$ is given by

$$\mathbf{b}_{\phi,\psi} = \begin{pmatrix} (S^*, \chi^{-1}(f^n)) \\ (H^*, \chi^{-1}(f^n)) \\ (Q^*, \chi^{-1}(f^n)) \\ (K^*, \chi^{-1}(f^n)) \\ (P^*, \zeta^{-1}(g^n)) \end{pmatrix}. \quad (\text{B.20})$$

The matrix $\mathbf{M}_{\phi,\psi}$ has the following structure:

$$\mathbf{M}_{\phi,\psi} = \begin{pmatrix} m_{11} & m_{12} & m_{13} & m_{14} & m_{15} \\ m_{21} & m_{22} & m_{23} & m_{24} & m_{25} \\ m_{31} & m_{32} & m_{33} & m_{34} & m_{35} \\ m_{41} & m_{42} & m_{43} & m_{44} & m_{45} \\ m_{51} & m_{52} & m_{53} & m_{54} & m_{55} \end{pmatrix}, \quad (\text{B.21})$$

where the entries are defined as follows:

Row 1–4, Columns 1–4:

$$\begin{aligned} m_{i1} &= c_{gs}(F_i^*, \hat{S}^*), & m_{i2} &= c_{ga}(F_i^*, \hat{H}^*), \\ m_{i3} &= c_{gb}(F_i^*, \hat{Q}^*), & m_{i4} &= c_{go}(F_i^*, \hat{K}^*), \\ \text{with } F_1^* &= S^*, F_2^* = H^*, F_3^* = Q^*, F_4^* = K^*, \\ \text{and diagonal corrections: } m_{ii} &\rightarrow 1 + m_{ii} \text{ for } i = 1, 2, 3, 4. \end{aligned}$$

Column 5:

$$\begin{aligned} m_{15} &= c_{go}(S^*, \hat{K}^*), \\ m_{25} &= c_{go}(H^*, \hat{K}^*), \\ m_{35} &= c_{go}(Q^*, \hat{K}^*), \\ m_{45} &= c_{go}(K^*, \hat{K}^*), \\ m_{55} &= 1 - (P^*, \Lambda_{P^*}). \end{aligned}$$

Row 5, Columns 1–4:

$$m_{51} = m_{52} = m_{53} = 0, \quad m_{54} = -(P^*, \Lambda_{P^*}). \quad (\text{B.22})$$

Once these scalar values are determined, the full field variables ϕ^{n+1} and ψ^{n+1} are recovered through substitution back into Equations (B.14)–(B.15).

Remark 6 (CC-MSAV-BDF1 scheme differences). *We enumerate the components that differ for the CC-MSAV-BDF1 scheme. For the remaining components, the derivation follows the same format, with extrapolation terms replaced by the corresponding variables from the previous time step.*

The explicit part of the Allen–Cahn equation on the right-hand side, de-

noted by f^n , becomes:

$$\begin{aligned}
f^n = & \frac{\phi^n}{\Delta t} - M_\phi \left\{ \left(\theta + \gamma_{bend} \frac{3\sqrt{2}}{4\varepsilon} \right) \Delta\phi^n \right. \\
& + \gamma_{surf} \frac{3\sqrt{2}}{2} \left[V^n + \int_{\Omega} S(\phi^n)(-\phi^n) d\mathbf{x} \right] S(\phi^n) \\
& + \gamma_{area} \left[U^n + \int_{\Omega} H(\phi^n)(-\phi^n) d\mathbf{x} \right] H(\phi^n) \\
& + \gamma_{bend} \frac{3\sqrt{2}}{8\varepsilon} \left[W^n + \int_{\Omega} Q(\phi^n)(-\phi^n) d\mathbf{x} \right] Q(\phi^n) \\
& + \left. \left[Z^n + \int_{\Omega} K(\phi^n, \psi^n)(-\phi^n) d\mathbf{x} \right. \right. \\
& \left. \left. + \int_{\Omega} P(\phi^n, \psi^n)(-\psi^n) d\mathbf{x} \right] K(\phi^n, \psi^n) \right\}. \tag{B.23}
\end{aligned}$$

The explicit part of the Cahn–Hilliard equation on the right-hand side, denoted by g^n , becomes:

$$g^n = \frac{\psi^n}{\Delta t} - \lambda \Delta \psi^n + \nabla \cdot (M_\psi(\phi^n) \nabla \tilde{\nu}^{n+1}), \tag{B.24}$$

where $\tilde{\nu}^{n+1}$, the explicit portion of the chemical potential, is defined as

$$\begin{aligned}
\tilde{\nu}^{n+1} = & \left[Z^n + \int_{\Omega} K(\phi^n, \psi^n)(-\phi^n) d\mathbf{x} \right. \\
& \left. + \int_{\Omega} P(\phi^n, \psi^n)(-\psi^n) d\mathbf{x} \right] P(\phi^n, \psi^n). \tag{B.25}
\end{aligned}$$

One of the coefficients for the operator χ is modified to:

$$C_{1,\chi} = \frac{1}{\Delta t} + M_\phi \gamma_{surf} \frac{3\sqrt{2}\beta}{4\varepsilon}. \tag{B.26}$$

The operator for the Cahn–Hilliard equation, ζ , is modified to:

$$\zeta(\psi) := \left(\frac{1}{\Delta t} - \lambda \Delta \right) \psi. \tag{B.27}$$

Remark 7 (Differences in the Classical–MSAV–BDF2 Scheme). *We summarize the components that differ in the Classical MSAV BDF2 formulation. The only modifications occur in the Cahn–Hilliard part of the scheme.*

First, the right-hand side g^n , which collects all explicit contributions, is replaced by

$$g^n = \frac{4\psi^n - \psi^{n-1}}{2\Delta t} + \nabla \cdot (M_\psi(\phi^{*,n+1}) \nabla \tilde{\nu}^{n+1}), \quad (\text{B.28})$$

where $\tilde{\nu}^{n+1}$, the explicit portion of the chemical potential, is defined as

$$\begin{aligned} \tilde{\nu}^{n+1} = & -\lambda\psi^{*,n+1} \\ & + \frac{1}{3} \left[4Z^n - Z^{n-1} + \int_{\Omega} K(\phi^{*,n+1}, \psi^{*,n+1}) (-4\phi^n + \phi^{n-1}) d\mathbf{x} \right. \\ & \left. + \int_{\Omega} P(\phi^{*,n+1}, \psi^{*,n+1}) (-4\psi^n + \psi^{n-1}) d\mathbf{x} \right] P(\phi^{*,n+1}, \psi^{*,n+1}). \end{aligned} \quad (\text{B.29})$$

Second, the linear operator associated with the Cahn–Hilliard equation is modified to

$$\zeta(\psi) := \left(\frac{3}{2\Delta t} - \lambda \nabla \cdot (M_\psi(\phi^{*,n+1}) \nabla) \right) \psi. \quad (\text{B.30})$$

Remark 8 (Differences in the Classical–MSAV–BDF1 Scheme). *Similarly, we summarize the differences in the Classical MSAV BDF1 formulation relative to the CC–MSAV BDF1 scheme.*

First, the right-hand side g^n , which collects all explicit contributions, is replaced by

$$g^n = \frac{\psi^n}{\Delta t} + \nabla \cdot (M_\psi(\phi^n) \nabla \tilde{\nu}^{n+1}), \quad (\text{B.31})$$

where $\tilde{\nu}^{n+1}$, the explicit portion of the chemical potential, is defined as

$$\begin{aligned} \tilde{\nu}^{n+1} = & -\lambda\psi^n \\ & + \left[Z^n + \int_{\Omega} K(\phi^n, \psi^n) (-\phi^n) d\mathbf{x} \right. \\ & \left. + \int_{\Omega} P(\phi^n, \psi^n) (-\psi^n) d\mathbf{x} \right] P(\phi^n, \psi^n). \end{aligned} \quad (\text{B.32})$$

Second, the linear operator is modified to

$$\zeta(\psi) := \left(\frac{1}{\Delta t} - \lambda \nabla \cdot (M_\psi(\phi^n) \nabla) \right) \psi. \quad (\text{B.33})$$

Algorithm 1 BDF2 MSAV Solution Procedure for Coupled Allen–Cahn–Cahn–Hilliard System

- 1: **Input:** Previous solutions $\phi^n, \phi^{n-1}, \psi^n, \psi^{n-1}$; SAVs V^n, U^n, W^n, Z^n and their $(n-1)$ values
 - 2: **Output:** Updated fields ϕ^{n+1}, ψ^{n+1} and SAVs at time $n+1$
 - 3:
 - 4: **Preprocessing:**
 - 5: Compute extrapolations $\phi^{*,n+1} = 2\phi^n - \phi^{n-1}$, $\psi^{*,n+1} = 2\psi^n - \psi^{n-1}$
 - 6: Evaluate basis functions S^*, H^*, Q^*, K^*, P^* at extrapolated values
 - 7:
 - 8: **Linear System Setup:**
 - 9: Compute RHS vectors f^n and g^n using explicit terms
 - 10: Solve elliptic problems: $\hat{f}^n = \chi^{-1}(f^n)$ and $\hat{g}^n = \zeta^{-1}(g^n)$
 - 11: For each basis function $F \in \{S^*, H^*, Q^*, K^*, P^*\}$:
 - 12: Solve $\hat{F} = \chi^{-1}(F)$ or $\Lambda_{P^*} = \zeta^{-1}(\nabla \cdot (M_\psi(\phi^{*,n+1}) \nabla P^*))$
 - 13:
 - 14: **Reduced System Solution:**
 - 15: Assemble 5×5 matrix $\mathbf{M}_{\phi,\psi}$ and vector $\mathbf{b}_{\phi,\psi}$
 - 16: Solve dense system: $\mathbf{M}_{\phi,\psi} \cdot [\tilde{B}, \tilde{C}, \tilde{D}, \tilde{E}, \tilde{G}]^T = \mathbf{b}_{\phi,\psi}$
 - 17:
 - 18: **Field Recovery:**
 - 19: Reconstruct ϕ^{n+1} using Equation (B.14) with computed integrals
 - 20: Reconstruct ψ^{n+1} using Equation (B.15) with computed integrals
 - 21:
 - 22: **SAV Update:**
 - 23: Update SAVs using
- $$V^{n+1} = \tilde{B} + \frac{1}{3} \left(4V^n - V^{n-1} + \int_{\Omega} S(\phi^{*,n+1})(-4\phi^n + \phi^{n-1}) d\mathbf{x} \right) \quad (\text{B.34})$$
- and similarly for others
- 24:
 - 25: **Return** $\phi^{n+1}, \psi^{n+1}, V^{n+1}, U^{n+1}, W^{n+1}, Z^{n+1}$
-

Appendix C. Fast Direct Solver for the Discretized Equations

To solve the linear system $\chi\phi = \mathbf{f}$, we employ a fast direct solver based on spectral diagonalization.

Constant-coefficient elliptic operators on rectangular domains can be diagonalized using fast orthogonal transforms depending on the boundary conditions: FFT for periodic, DST for homogeneous Dirichlet, and DCT for homogeneous Neumann boundaries. These transform-based Poisson solvers are classical [28, 30, 13, 22]. Efficient direct solvers for separable elliptic problems have also been developed in the spectral and spectral-element settings [25, 12]. Here, we apply the same idea to *fourth-order* constant-coefficient elliptic operators discretized with cell-centered finite differences and homogeneous Neumann boundary conditions.

Since χ is a polynomial in the discrete Laplacian Δ_h , it shares the same eigenvectors and is therefore diagonalizable by the DCT. Let h denote the grid spacing and (m, n) the grid size. The eigenvalues of Δ_h for cell-centered grids with Neumann BCs are

$$\lambda_{ij} = -\frac{4}{h^2} \left[\sin^2\left(\frac{\pi i}{2m}\right) + \sin^2\left(\frac{\pi j}{2n}\right) \right], \quad i = 0, \dots, m-1, \quad j = 0, \dots, n-1, \quad (\text{C.1})$$

with $\lambda_{00} = 0$ corresponding to the constant mode. The operator χ then has eigenvalues

$$\lambda_{\chi,ij} = C_{1,\chi} - C_{2,\chi}\lambda_{ij} + C_{3,\chi}\lambda_{ij}^2, \quad (\text{C.2})$$

where coefficients $C_{k,\chi}$ depend on the form of χ in Eq. (B.7).

The solver proceeds as:

1. Apply a forward 2D DCT: $\hat{\mathbf{f}} = \text{DCT}(\mathbf{f})$.
2. Compute $\hat{\phi} = \hat{\mathbf{f}}/\lambda_\chi$, handling the zero mode by enforcing $\sum \mathbf{f} = 0$.
3. Apply an inverse DCT: $\phi = \text{IDCT}(\hat{\phi})$.

This direct $O(N^2 \log N)$ solver achieves machine precision and eliminates iterative convergence issues. While similar procedures apply for periodic or Dirichlet boundaries (using FFT or DST), this DCT-based formulation provides an efficient and straightforward approach to fourth-order elliptic equations with homogeneous Neumann conditions.

Appendix D. Spatial Discretization: Complete Technical Framework

In this appendix, we collect the technical details of the staggered-grid, cell-centered finite difference discretization used in Section 3.4. We record here the grid layout, discrete operators, summation-by-parts identities, and the verification of structure-preserving properties used throughout the paper.

Appendix D.1. Grid Structure and Discrete Function Spaces

We consider the rectangular domain $\Omega = (0, L_x) \times (0, L_y)$, where $L_x = mh$ and $L_y = nh$, with uniform grid spacing $h > 0$. Following standard staggered-grid constructions, we define the one-dimensional grids

$$E_m = \{ih \mid i = 0, \dots, m\}, \quad (\text{D.1})$$

$$C_m = \{(i - \frac{1}{2})h \mid i = 1, \dots, m\}, \quad (\text{D.2})$$

$$\bar{C}_m = \{(i - \frac{1}{2})h \mid i = 0, \dots, m + 1\}, \quad (\text{D.3})$$

representing edge-centered points, cell centers, and cell centers including ghost points, respectively. Analogous definitions apply in the y -direction.

East–west faces are indexed by $i + \frac{1}{2}$, $i = 0, \dots, m$, and north–south faces by $j + \frac{1}{2}$, $j = 0, \dots, n$.

Based on these grids, we define the discrete function spaces

$$\mathcal{C}_{m \times n} = \{\phi : C_m \times C_n \rightarrow \mathbb{R}\}, \quad (\text{D.4})$$

$$\bar{\mathcal{C}}_{m \times n} = \{\phi : \bar{C}_m \times \bar{C}_n \rightarrow \mathbb{R}\}, \quad (\text{D.5})$$

$$\mathcal{E}_{m \times n}^{\text{ew}} = \{f : E_m \times C_n \rightarrow \mathbb{R}\}, \quad (\text{D.6})$$

$$\mathcal{E}_{m \times n}^{\text{ns}} = \{g : C_m \times E_n \rightarrow \mathbb{R}\}. \quad (\text{D.7})$$

In component form, we write

$$\phi_{i,j} = \phi(x_i, y_j), \quad f_{i+\frac{1}{2},j} = f(x_{i+\frac{1}{2}}, y_j), \quad g_{i,j+\frac{1}{2}} = g(x_i, y_{j+\frac{1}{2}}),$$

where $x_i = (i - \frac{1}{2})h$ and $y_j = (j - \frac{1}{2})h$.

Appendix D.2. Discrete Difference and Averaging Operators

We now introduce the discrete operators used throughout the paper.

Appendix D.2.1. Edge-to-Center Differences

For face-centered quantities, we define

$$(d_x f)_{i,j} = \frac{f_{i+\frac{1}{2},j} - f_{i-\frac{1}{2},j}}{h}, \quad f \in \mathcal{E}_{m \times n}^{\text{ew}}, \quad (\text{D.8})$$

$$(d_y g)_{i,j} = \frac{g_{i,j+\frac{1}{2}} - g_{i,j-\frac{1}{2}}}{h}, \quad g \in \mathcal{E}_{m \times n}^{\text{ns}}. \quad (\text{D.9})$$

These operators provide a conservative discretization of the divergence.

Appendix D.2.2. Center-to-Edge Operators

For $\phi \in \mathcal{C}_{m \times n}$, we define the averaging operators

$$(A_x \phi)_{i+\frac{1}{2},j} = \frac{1}{2}(\phi_{i,j} + \phi_{i+1,j}), \quad (\text{D.10})$$

$$(A_y \phi)_{i,j+\frac{1}{2}} = \frac{1}{2}(\phi_{i,j} + \phi_{i,j+1}), \quad (\text{D.11})$$

and the discrete gradients

$$(D_x \phi)_{i+\frac{1}{2},j} = \frac{\phi_{i+1,j} - \phi_{i,j}}{h}, \quad (\text{D.12})$$

$$(D_y \phi)_{i,j+\frac{1}{2}} = \frac{\phi_{i,j+1} - \phi_{i,j}}{h}. \quad (\text{D.13})$$

Appendix D.2.3. Discrete Laplacian

We define the discrete Laplacian by composing divergence and gradient operators:

$$(\Delta_h \phi)_{i,j} = (d_x D_x \phi)_{i,j} + (d_y D_y \phi)_{i,j} \quad (\text{D.14})$$

$$= \frac{1}{h^2} (\phi_{i+1,j} + \phi_{i-1,j} + \phi_{i,j+1} + \phi_{i,j-1} - 4\phi_{i,j}). \quad (\text{D.15})$$

Appendix D.3. Discrete Inner Products and Norms

For cell-centered functions $\phi, \psi \in \mathcal{C}_{m \times n}$, we use the discrete L^2 inner product

$$(\phi, \psi)_h = h^2 \sum_{i=1}^m \sum_{j=1}^n \phi_{i,j} \psi_{i,j}.$$

For face-centered quantities, we define

$$[f, g]_{\text{ew},h} = \frac{h^2}{2} \sum_{i,j} (f_{i+\frac{1}{2},j} g_{i+\frac{1}{2},j} + f_{i-\frac{1}{2},j} g_{i-\frac{1}{2},j}), \quad (\text{D.16})$$

$$[f, g]_{\text{ns},h} = \frac{h^2}{2} \sum_{i,j} (f_{i,j+\frac{1}{2}} g_{i,j+\frac{1}{2}} + f_{i,j-\frac{1}{2}} g_{i,j-\frac{1}{2}}). \quad (\text{D.17})$$

We then define the discrete H^1 norm

$$\|\nabla_h \phi\|_2^2 = [D_x \phi, D_x \phi]_{\text{ew},h} + [D_y \phi, D_y \phi]_{\text{ns},h}.$$

Appendix D.4. Boundary Conditions

Throughout the paper, we impose homogeneous Neumann boundary conditions. We enforce these using ghost cells by setting

$$\phi_{0,j} = \phi_{1,j}, \quad \phi_{m+1,j} = \phi_{m,j}, \quad \phi_{i,0} = \phi_{i,1}, \quad \phi_{i,n+1} = \phi_{i,n}.$$

With this choice, the face-centered normal derivatives vanish at the boundary:

$$(D_x \phi)_{\frac{1}{2},j} = (D_x \phi)_{m+\frac{1}{2},j} = 0, \quad (D_y \phi)_{i,\frac{1}{2}} = (D_y \phi)_{i,n+\frac{1}{2}} = 0.$$

Appendix D.5. Summation-by-Parts Identities

The staggered-grid operators satisfy discrete summation-by-parts identities. For $\phi \in \bar{\mathcal{C}}_{m \times n}$, $f \in \mathcal{E}_{m \times n}^{\text{ew}}$, and $g \in \mathcal{E}_{m \times n}^{\text{ns}}$, we have

$$[D_x \phi, f]_{\text{ew},h} = -(\phi, d_x f)_h + B_x(\phi, f), \quad (\text{D.18})$$

$$[D_y \phi, g]_{\text{ns},h} = -(\phi, d_y g)_h + B_y(\phi, g), \quad (\text{D.19})$$

where B_x and B_y denote boundary contributions.

Under the homogeneous Neumann conditions imposed above and vanishing boundary fluxes, these boundary terms are zero. We therefore obtain the discrete Green's identity

$$[D_x \phi, D_x \psi]_{\text{ew},h} + [D_y \phi, D_y \psi]_{\text{ns},h} = -(\phi, \Delta_h \psi)_h = -(\Delta_h \phi, \psi)_h.$$

In particular,

$$(\phi, \Delta_h \phi)_h = -\|\nabla_h \phi\|_2^2 \leq 0.$$

Appendix D.6. Exact Mass Conservation

Because all fluxes are discretized in conservative form, mass conservation follows immediately.

Theorem Appendix D.1. *For any fluxes $f \in \mathcal{E}_{m \times n}^{\text{ew}}$ and $g \in \mathcal{E}_{m \times n}^{\text{ns}}$ satisfying the boundary conditions,*

$$h^2 \sum_{i,j} (d_x f + d_y g)_{i,j} = 0.$$

Proof. The result follows by telescoping sums in each coordinate direction. The remaining details are straightforward and omitted. \square

Appendix D.7. Structure-Preserving Discretization of Nonlinear Terms

We now verify the key structure-preserving properties used in the energy analysis.

Appendix D.7.1. Quadratic Face Averaging

We define the quadratic face-averaging operators

$$A_x^{(q)}(\phi^2)_{i+\frac{1}{2},j} = \frac{1}{3}(\phi_{i+1,j}^2 + \phi_{i+1,j}\phi_{i,j} + \phi_{i,j}^2), \quad (\text{D.20})$$

$$A_y^{(q)}(\phi^2)_{i,j+\frac{1}{2}} = \frac{1}{3}(\phi_{i,j+1}^2 + \phi_{i,j+1}\phi_{i,j} + \phi_{i,j}^2). \quad (\text{D.21})$$

A direct computation shows that the discrete product rule

$$D_x(\phi^3) = 3A_x^{(q)}(\phi^2)D_x\phi, \quad D_y(\phi^3) = 3A_y^{(q)}(\phi^2)D_y\phi$$

holds exactly. Combining this identity with the SBP property yields

$$(\phi^3, \Delta_h\phi)_h = -3(\phi^2, |\nabla_h\phi|^2)_h.$$

Appendix D.7.2. Variable Mobility Flux

We discretize the variable-mobility Cahn–Hilliard flux as

$$\nabla \cdot (M_\psi \nabla \nu) = d_x(M_\psi(A_x\phi)D_x\nu) + d_y(M_\psi(A_y\phi)D_y\nu).$$

Using SBP, we obtain

$$(\nu, \nabla \cdot (M_\psi \nabla \nu))_h = -\|\sqrt{M_\psi} \nabla_h \nu\|_2^2 \leq 0.$$

Appendix D.7.3. Nonlocal Bending Term

Finally, we discretize the nonlocal bending contribution as

$$[\phi|\nabla\phi|^2]_{i,j} = \phi_{i,j} \left[\frac{|D_x\phi|_{i+\frac{1}{2},j}^2 + |D_x\phi|_{i-\frac{1}{2},j}^2}{2} + \frac{|D_y\phi|_{i,j+\frac{1}{2}}^2 + |D_y\phi|_{i,j-\frac{1}{2}}^2}{2} \right], \quad (\text{D.22})$$

$$[\nabla \cdot (\phi^2 \nabla \phi)]_{i,j} = d_x((A_x\phi^2)D_x\phi)_{i,j} + d_y((A_y\phi^2)D_y\phi)_{i,j}. \quad (\text{D.23})$$

A careful but routine application of SBP then yields the discrete bending-energy identity stated in the main text.

Appendix E. Selection of Stabilization Parameters

The stabilization parameters θ and λ require careful selection to ensure energy stability, monotonic energy dissipation, and mass conservation. We conducted systematic parameter testing to determine the minimum viable values that satisfy these criteria for interface width $\varepsilon = 0.03125$ and spatial resolution $N = 256$.

Allen-Cahn Stabilization Parameter θ . The Allen-Cahn stabilization parameter θ provides artificial dissipation in the chemical potential to control interface dynamics. Initial validation tests over 100 time steps identified $\theta = 1.5$ as the minimum value ensuring energy monotonicity (after initial transients) and mass conservation to high precision. This value is used for all standard simulations. For robustness tests involving aggressive morphological changes (Section 4.4), we increase θ to 30 to maintain stability under more challenging interfacial dynamics.

Cahn-Hilliard Stabilization Parameter λ . The Cahn-Hilliard stabilization parameter λ appears in the IMEX splitting term $\lambda(\Delta\psi^{n+1} - \Delta\psi^{*,n+1})$, where $\psi^{*,n+1}$ is a second-order extrapolation. Initial testing identified $\lambda = 4.5 \times 10^4$ as minimally sufficient for short simulations, but extended tests with various initial geometries revealed that λ must be larger to maintain stability across diverse scenarios. We therefore adopt $\lambda = 10^5$ for all simulations to robustly accommodate different test cases.

Appendix F. Generation of Smoothed Initial Conditions

The numerical experiments in Section 4.4 utilizing non-analytical initial geometries (triangle, star, incomplete hexagon, and crescent shape) require conversion from sharp interface profiles to smooth, diffuse interfaces suitable for phase field simulation. The sharp profiles, where the domain is partitioned into regions of $\phi = 1$ and $\phi = -1$, are relaxed into physically realistic and numerically stable starting conditions.

This smoothing is achieved by evolving the sharp initial condition, ϕ_{sharp} , for a short duration using the classical Cahn-Hilliard equation with constant mobility:

$$\frac{\partial\phi}{\partial t} = M\Delta \left(\frac{1}{\varepsilon}(\phi^3 - \phi) - \varepsilon\Delta\phi \right), \quad (\text{F.1})$$

subject to homogeneous Neumann boundary conditions. The mobility parameter $M = 0.01$ and time step $\Delta t = 1 \times 10^{-6}$ are selected to minimize interface migration while achieving numerical stability. These parameters limit the diffusive length scale to $O(\varepsilon)$ over the smoothing duration, preventing over-smoothing that would compromise the initial geometric features.

The smoothing simulation employs the same semi-implicit, first-order time-stepping scheme used in the main solver. The linear biharmonic term $(-M\varepsilon\Delta^2\phi)$ is treated implicitly, while the nonlinear term is explicit, resulting in linear, constant-coefficient biharmonic-type equations solved using the fast direct solver (Appendix C).

The smoothing evolution is run for a short total time $T_{\text{smooth}} = 10^{-5}$. Over this interval, the free energy decreases rapidly at early times and then approaches a plateau, indicating that the diffuse interface has reached its local equilibrium profile while the global geometric features remain essentially unchanged. The resulting smoothed interfaces exhibit transition layers consistent with the expected diffuse-interface thickness of the Cahn–Hilliard model, without altering the intended geometry. As a final preprocessing step, we clamp values outside the physical range by applying $\phi \leftarrow \max(-1, \min(1, \phi))$.

Appendix G. Simulation Parameters

This section details the parameters used for the numerical experiments presented in Section 4. Parameters that differ between growth and shrinkage scenarios are distinguished using subscripts g and s , respectively.

Table G.5: Parameter values used in benchmark simulations. Physical parameters are dimensionless.

Parameter	Symbol	Value
Physical Parameters		
Surface Tension	γ_{surf}	1.0
Bending Rigidity (Growth)	$\gamma_{\text{bend,g}}$	0.05
Bending Rigidity (Shrinkage)	$\gamma_{\text{bend,s}}$	1
Arc Length Constraint Penalty	γ_{area}	5×10^4
Osmotic Penalty (in)	γ_{in}	1×10^5
Osmotic Penalty (out)	γ_{out}	1×10^5
Equilibrium Conc. (in, Growth)	$\psi_{\text{in},g}$	0.65
Equilibrium Conc. (in, Shrinkage)	$\psi_{\text{in},s}$	0.1
Equilibrium Conc. (out)	ψ_{out}	0.8
Osmotic Baseline Constant (in)	β_{in}	0
Osmotic Baseline Constant (out)	β_{out}	0
Interface Width	ε	0.03125
Allen-Cahn Mobility	M_ϕ	1.0
Cahn-Hilliard Mobility Param.	M_0	0.5
Common Numerical Parameters		
Grid Resolution	N	256×256
Time Step	Δt	1×10^{-6}
Final Time	T	0.02
Numerical Parameters (MSAV Method)		
Allen-Cahn Stabilization	θ	1.5
Allen-Cahn Stabilization Parameter	β	0
Cahn-Hilliard Stabilization	λ	1×10^5
Numerical Parameters (NLMG Method)		
Convergence Tolerance	tol	1×10^{-8}
Minimum Refinement Level	minlevel	-8
Pre-smoothing Steps	presmooth	2
Post-smoothing Steps	postsmooth	2
Maximum Iterations	maxits	100